MODELING AND CHARACTERIZATION OF MATERIAL DEPOSITION STRATEGY IN
ADDITIVE MANUFACTURING

A thesis presented to the faculty of the Graduate School of Western Carolina University in
partial fulfillment of the requirements for the degree of Master of Science in Engineering
Technology

By

Md Saidur Rahman Roney

Advisor: Dr. AMM Nazmul Ahsan
Assistant Professor
School of Engineering and Technology

Committee Members:
Dr. Basel Alsayyed Ahmad, School of Engineering and Technology
Dr. Sudhir Kaul, School of Engineering and Technology

May 2023

ACKNOWLEDGEMENTS

TABLE OF CONTENTS

LIST OF TABLES

LIST OF FIGURES

ABSTRACT

MODELING AND CHARACTERIZATION OF MATERIAL DEPOSITION STRATEGY IN ADDITIVE MANUFACTURING

Md Saidur Rahman Roney, MSET

Western Carolina University, (April 2023)

Advisor: Dr. Nazmul Ahsan

The capability of producing complex-shaped objects, lightweight porous objects, and handling a wide range of materials such as metals, plastics, and resins allows Additive Manufacturing (AM) technologies as a viable alternative. Despite this extensive scope, defects such as warpage, delamination, cracks, porosity, and brittleness can be detrimental to the widespread use of AM. Such defects can be mitigated by manipulating the input process parameters depending on the AM technology that is being used. Since the AM technologies primarily use a layer-by-layer material deposition strategy, many of the build part properties and defects are influenced by the material deposition pattern in service. In this research, the effect of material deposition patterns on build part properties is studied for two different AM processes, namely, Laser Powder Bed Fusion (LPBF) and Fused Deposition Modeling (FDM). Two novel material deposition patterns are investigated in this study for LPBF and FDM processes, specifically using a scan pattern and an infill pattern respectively. In the LPBF process, residual stress is analyzed for multiple scan patterns by using the Finite Volume Method (FVM). Residual stress can be responsible for possible build part warpage and is greatly dependent on the thermal gradient generated on the part during

the layer-by-layer deposition. A novel scan pattern is designed to reduce the thermal gradient through a re-heating approach and by turning the scanning directions along both longitudinal and transverse directions in a periodic manner. Simulation results indicate that the proposed pattern can reduce the residual stress from the very first layer and maintain the minimum stress value through the build process as compared to the existing traditional Zigzag, Island Zigzag, and Spiral scan patterns that are commonly used. The simulation results are also comparable to studies in literature. The residual stress for the proposed pattern can be further investigated in the future by reversing the scanning direction and implying an overlap factor between two successive scan passes. On the other hand, in the FDM process, the compressive strength of the build part for the proposed infill pattern is measured and compared with the existing Zigzag infill pattern. The infill pattern in the AM technology provides a scope for producing lightweight porous objects, and its mechanical behavior varies based on structure types and manufacturing strategies. Thus, the novel infill pattern proposed in this study enhances some of the mechanical properties and may widen the scope of a designer's choice. The proposed infill pattern is an island type that combines the existing Zigzag and Honeycomb infill patterns such that the zigzag raster reflects the hexagonal cells oriented periodically along the island span. The experimental data demonstrate that the proposed infill pattern results in higher compressive strength and elastic modulus as compared to the Zigzag infill pattern for a similar relative infill density.

CHAPTER ONE: INTRODUCTION

1.1 Introduction

The manufacturing technology paces up the world economy and resolves obstacles to meet customer demand at a reasonable price. Products can be manufactured through additive, subtractive, or forming processes. Additive manufacturing is a convenient technology that opens the gateway to producing any intricate shaped objects that, in many cases, are challenging to produce by using manufacturing technologies. Furthermore, additive manufacturing process reduces material wastage through maintaining higher dimensional accuracy of the product.

In additive manufacturing technology, the material is deposited through layer-by-layer fashion according to the CAD (Computer-Aided Design) model, where each layer gets fused with the previous layer [1]. This technology is capable of working with several materials, including metals, liquid resins, and plastic polymers [1]. Metal parts are fabricated by using Powder Bed Fusion (PBF), Direct Energy Deposition (DED) and Metal Binder Jetting technology, familiar as Metal Additive Manufacturing (MAM) technology. On the other hand, plastic polymer objects are usually printed by using Fused Deposition Modeling (FDM) technology.

Among different MAM technologies this research focuses on the Laser Powder Bed Fusion (LPBF) technology, where metal parts are fabricated in a powder bed through layer-by-layer material addition process [1]. In this process, a recoater spreads a thin layer of metal powder over the powder bed at each layer allowing the heat source, such as the laser beam to scan over the powder bed to build the part according to the information of the corresponding layer described in the CAD model [1]. During scanning, to fill up the bulk material, the laser beam follows a pre-described pattern known as scan pattern.

Despite the capability of additive manufacturing technology to produce intricate shaped objects with higher accuracy, the parts/product suffers from several common defects such as porosity, delamination, crack, warpage and brittleness which are now drawing the attention of researchers to pave the maturity of this technology. The amount of these defects can be reduced by manipulating the process input parameters like powder quality, laser power, scanning speed, hatch spacing, scanning length, scan pattern, scanning direction, and bed pre-heating temperature. The metal powders produced by gas atomization technology have a topology of fine spherical shape that is perfect for reducing porosity and improving surface roughness [2]. A possible way to achieve near optimum values for laser power and scanning speed to improve cracking, delimitation, and porosity is to frequently monitor the build part density [3]. However, this research concentrates on the development of residual stress in build part as it is responsible for possible part warpage. It is challenging to predict the proper scan patterns and scanning directions to improve residual stress and other mechanical properties. Several research studies had been carried out over the past decades to figure out the optimal solution to address this issue [3-8].

In Laser Powder Bed Fusion (LPBF), the heat source moves along the part build, and the powder metal gets melted and fused with the previous layer [2]. The tiny melt pool generated due to the interaction of the laser beam solidifies rapidly through dissipating the thermal energy in its surroundings. This process is governed by the neighboring temperatures of the melt pool and increases the thermal gradient of the build part [2]. Material expansion and shrinkage takes place due to the localized heating and rapid solidification, producing tensile and compressive residual stress over the part which is responsible for possible part deformation upon printing [2]. Some post-processing techniques are applied after printing the build part to eliminate residual stress, such as re-heating through annealing process. Ideally, a great solution for inhibiting the residual

stress development in build part is to achieve the uniform thermal distribution and to increase the overall build part temperature for preventing rapid solidification of melt pool [2]. Modifying and finding an optimum scan pattern may be an excellent solution to achieve even distribution of thermal energy i.e., reducing the thermal gradient of build part. Several research studies were conducted to figure out the residual stresses for specific scan patterns [3-8].

Furthermore, it is observed that due to the rapid solidification of melt-pool columnar grains are developed along the build direction, that governs the brittleness of the build part [2]. In order to prevent the development of columnar grains through replacing it with equiaxial grains that restores ductility, the thermal gradient of the build part should be reduced and the rapid solidification of melt pool should be inhibited [2]. The above discussion represents that the optimization of the scan pattern widens the scope for minimizing the residual stress and improving the product's microstructure [9].

On the other hand, FDM technology uses 3D CAD models to deposit plastic material in a layer-by-layer manner through melting the plastic filaments by a nozzle. This layer-by-layer material deposition strategy broadens the scope of producing lightweight porous objects through replacing the bulk material of a solid body inside the skin with different types of lattice cells, that are familiar as infill patterns. There are fewer types of available infill patterns in commercial slicing software, and the mechanical behavior of these infill patterns varies based on their type, density, and manufacturing strategy. The printed object's mechanical response is dependent on the infill pattern and infill density in use, and the limitations of available infill pattern types confines designers' choices to manipulate the mechanical behavior of the printed objects. As the application of an object seeks specific mechanical properties, developing novel infill patterns may widen the scope of customizing the mechanical properties of the printed parts.

The thesis consists of two studies namely developing scan pattern for LPBF process and developing infill pattern for FDM process. In chapter 3, a novel scan patten is developed based on uniform thermal distribution and reheating strategy. The residual stress of the proposed scan pattern is analyzed by using Finite Volume Method (FVM) and compared with other existing scan patterns. In chapter 4, a novel island-type infill pattern is developed that combines the existing Zigzag pattern with the Honeycomb pattern such that the zigzag raster reflects the hexagonal cells arranged periodically along the island span. As it is difficult to print all sides of the hexagonal cells in a single layer due to the non-continuous toolpath and non-uniform cell walls, the proposed pattern takes the advantage of the Zigzag pattern through generating a continuous toolpath for hexagonal cells in each island, increasing the manufacturability of the pattern. Although the hexagonal cells in the proposed pattern contain some overlap among the adjacent lattice cells and islands, it provides the possibility of combining both patterns. Furthermore, the stack of alternating layers generates a weave pattern that distributes the structural integrity along both the longitudinal and transverse directions. The mechanical behavior, such as the compressive strength of the proposed infill pattern, is explored through compression tests.

1.2 Objectives

In this thesis, the objective is to develop material deposition strategies for two different AM technologies and to study their effect as described below:

1. Developing a novel scan pattern and numerically investigating its effect on residual stress..

2. Developing a novel hybrid infill pattern and exploring its mechanical behavior, through compression tests.

Both studies reveal the nature of the proposed patterns and their superior performance over other existing patterns.

CHAPTER TWO: LITERATURE REVIEW

2.1 Additive Manufacturing Technology

Additive Manufacturing (AM) technology removes the barrier of engineering design and opens the gateway for manufacturing any complex shaped object with higher dimensional accuracy. This technology was first invented by Chuck Hull in 1980s in the form of 3D printing, denoted as stereo-lithography, and its commercial use started in 1987 [5]. AM usually uses the 3D Computer-Aided Design (CAD) model information to deposit material through layer-by-layer manner. In this process, the CAD model is converted into a stereolithography (.stl) file which represents a chain of linked triangles to describe the surface geometry of the CAD file. The .stl file is then sliced into multiple layers along the build direction, and the 3D printer uses that layers information to print the 3D model [1].

With the development of technology, several categories of 3D printing technologies have been invented, and their classification is presented in Figure 1 based on the working material [1].
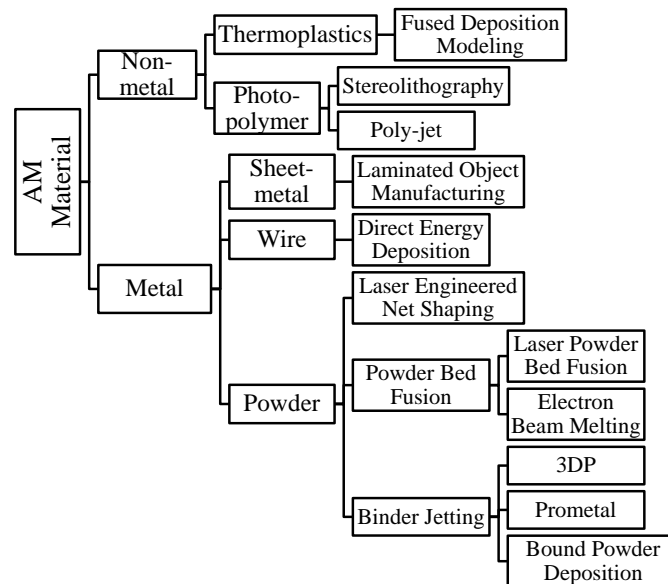
Figure 1: Classification of Additive Manufacturing [1, 10]

Usually, plastic models are produced using the Fused Deposition Modeling (FDM) process, where the plastic filament is deposited into the printing bed through melting at the extruder nozzle and gets fused with the previous layer. It is a cheap process and produces low resolution part [1].

In Stereolithography (SL), photosensitive liquid polymers such as photosensitive resins get solidified with the influence of UV light at each layer. The layer thickness of the printed part may vary due to the variation of the resin viscosity [1].

In Laminated Object Manufacturing (LOM), laminated sheet metals are sheared by laser or other means according to the layer information. After that the sheet metal layers are bonded together with the application of pressure and heat. It is a low-cost process that can be used to build large prototypes, but material wastage is higher in this process [1].

On the other hand, metal parts are usually fabricated using powdered metals as the build material. For Selective Laser Sintering (SLS) and Electron Beam Melting (EBM) processes, the recoater spreads a thin layer of powder metal on the powder bed. After that, a moving point heat source (laser or Electron Beam for SLS and EBM, respectively) travels on the powder bed that selectively melts and fuses the powder with the previous layer according to the layer information of the CAD model. After finishing the scanning of a layer, the powder bed is shifted down according to the layer thickness, and the recoater spreads another layer of powder metal for the next layer. Besides, in Laser Engineered Net Shaping (LENS) (usually known as Direct Energy Deposition (DED)) technology, the metal powder is injected through a nozzle and gets melted subsequently by a laser or Electron Beam at each layer [1, 2]. Aside from these technologies, another method worth mentioning does not use any heat source to melt the powder. Instead, it uses a binding agent deposited on the powder layer, and thus the part is built up through layer by layer.

This technology is called the binder jetting process, and it can work with a wide variety of materials [1].

2.2 Metal Additive Manufacturing

Nowadays, metals and their alloys play an important role in engineering applications for their suitable properties. From the discussion at section 2.1, metal parts can be fabricated by using SLS, EBM, or DED technology. DED is usually used for repairing parts because of its capability to handle the damaged part as a substrate on the build plate [2, 11]. Furthermore, it is not used to print whole parts due to its low accuracy and the requirement of post-processing of the printed parts [12]. Powder bed fusion (PBF) technology like SLS and EBM is widely used for fabricating metal parts. In EBM technology, the powder bed platform's preheating temperature is maintained around 80% of the melting temperature, while in SLS, it is around 90°C [2, 12]. In addition, the build chamber of EBM is in a vacuum, and the build chamber in SLS is purged with Argon gas, which affects the cooling process of molten metal during the part building process [2].

In PBF processes, rapid solidification takes place due to its small melt pool size and the comparative lower surrounding temperature. The uneven heating originated from the melting and cooling of small regions results in a temperature difference called a thermal gradient. For EBM, the thermal gradient is low due to its higher bed pre-heating temperature, and the vacuum build chamber reduces the heat loss that impedes rapid cooling of the melt pool. On the other hand, in SLS, the thermal gradient is higher due to lower bed pre-heating temperature, and Argon gas purging into the build chamber causes the convection heat transfer [2, 12].
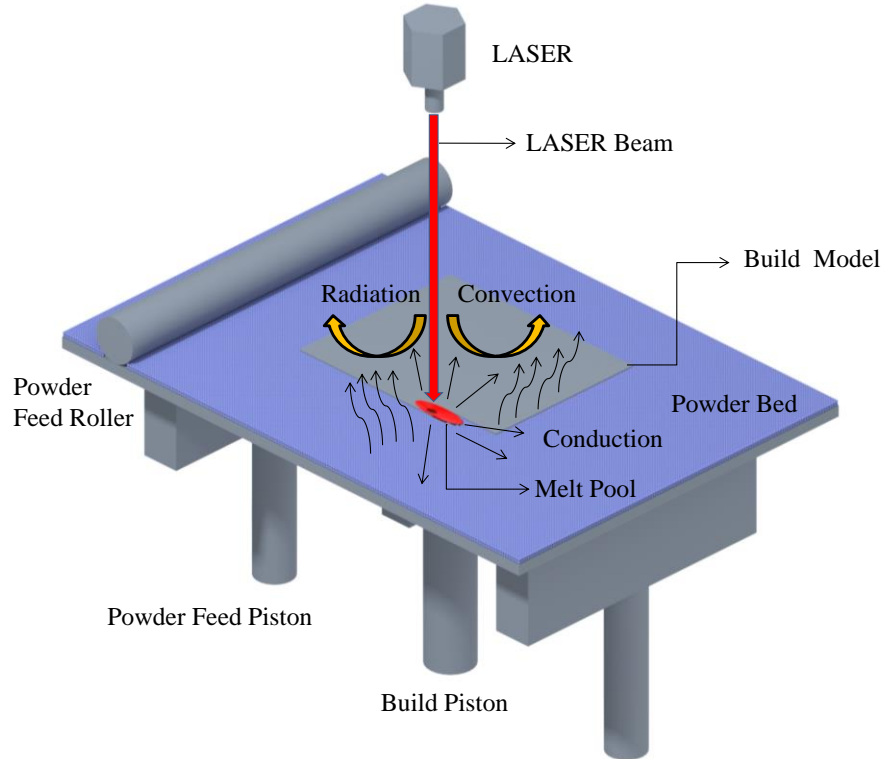
Figure 2: LPBF System.

2.2.1 Defects of Metal Printed Parts

The parts produced using PBF technology may contain common defects such as porosity, crack, delamination, poor surface quality, warpage, and brittleness [2]. Tiny pores with less than 100µm in diameter can develop in the build part due to the higher thermal gradient, rapid cooling, or entrapped gas [13]. In addition, the deep and narrow melt pool generated for high laser power causes molten metal to evaporate which develops recoil pressure and key-holes, increasing the porosity of the build part [2, 10]. Besides, delamination and cracking may occur from a lack of fusion of a frequent layer with its previous layer, results from the lack of deposition energy that depends on laser power and scanning speed [2, 13]. On the other hand, the powder quality dramatically influences the above defects, such as low packing density powder may produce porosity [13]. Nowadays, gas-atomized technology produces high-quality powders that are

extremely small (10µm~300µm diameter), spherical-shaped, and pure (low oxygen content) [14]. Some other defects, such as the warpage of the build part, results from the stored residual stress developed due to the higher thermal gradient. Whenever the molten metal solidifies in the melt pool, it shrinks and imparts a mechanical force on the surrounding regions of the melt pool, while the moving heat source is responsible for uneven heating resulting in non-uniform expansion of the build part. The consequent internal stress is responsible for the part distortion during printing, upon removal from the production bed, or in service. In order to remove these defects, some post-processing actions such as heat treatment or hot isostatic pressing are executed on the printed build part [2].

2.2.2 Residual Stress

Residual stress develops for higher thermal gradient generated from uneven heating and rapid cooling. The transient heating of the build part and the lower surrounding temperature governs the rapid solidification. As per discussion from 2.2.1, the associated non uniform expansion and shrinkage force causes the overall residual stress, which depends on the thermal history or thermal distribution and the build part temperature.
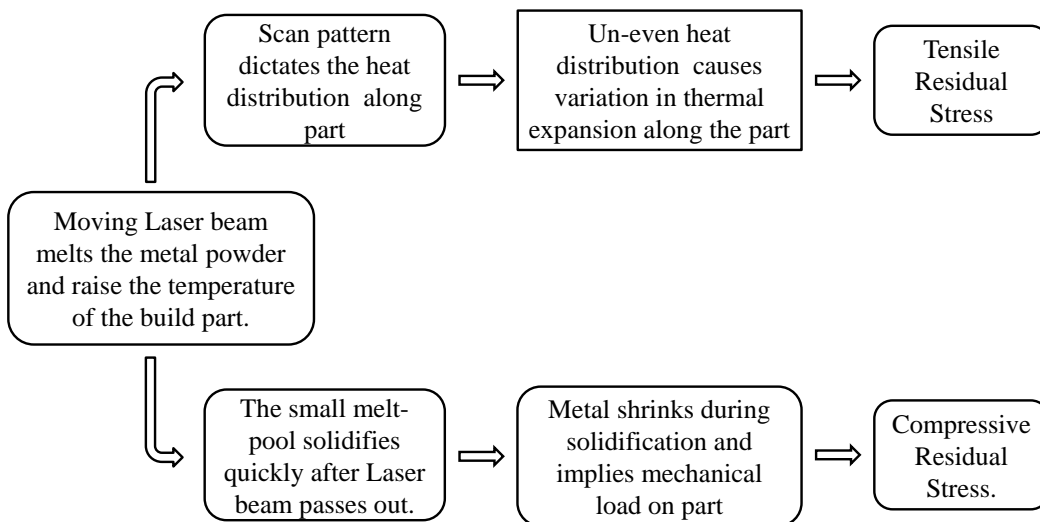
Figure 3: Development of Residual Stresses.

9

To eliminate the development of residual stress, the thermal gradient should be lower, and the rapid solidification of the melt pool should be inhibited. The higher temperature of the build part inhibits the rapid solidification of the melt pool, and the uniform thermal distribution lowers the thermal gradient, thus inhibiting the uneven thermal expansion or shrinkage of the build part. Furthermore, the residual stress developed by a scanning pass can be relieved by the reheating actions through mitigating the thermal gradient.

In Laser Powder Bed Fusion (LPBF) technology, to fill up the bulk material of the build part, the laser follows a pre-defined path and melts the metal powder along the path. This path is defined as the scan pattern. Optimizing the scan pattern broadens the scope of reducing the uneven distribution of thermal energy and thus the residual stress.

2.2.3 Residual Stress Calculation

The calculation of the residual stress is divided into two sections. Firstly, the thermal gradient for a specific scan pattern is calculated (Section 2.2.3.1). Secondly, the residual stress against that thermal gradient is analyzed (Section 2.2.3.2).

2.2.3.1 Thermal Model.

The numerical model in this simulation is a transient conduction heat transfer model that considers solid-liquid phase change by using the enthalpy method, variable thermo-physical properties, and three-dimensional additive layer formation. The bottom surface is considered as a constant temperature boundary condition that allows conduction heat transfer, while the four sides and top surfaces are considered for radiation and convection heat transfer. In addition, the heat transfer along the powder bed is considered as the conduction heat transfer. The governing equation for conduction heat transfer along the powder bed is described in Equation 1 [6, 8]:

$$\rho C_P \frac{\partial T}{\partial t} = \frac{\partial}{\partial x}\left(K_x \frac{\partial T}{\partial x}\right) + \frac{\partial}{\partial y}\left(K_y \frac{\partial T}{\partial y}\right) + \frac{\partial}{\partial z}\left(K_z \frac{\partial T}{\partial z}\right) + q \tag{1}$$

Here, ρ is material density; C_p is specific heat; T is temperature; t is time; q is the heat transfer for solid-liquid phase change; and K_x, K_y, and K_z are the thermal conductivity in the x, y, and z directions. The latent heat absorbed during the solidification of melt pool is calculated by using Equations 2 and 3 [8]:

$$q = -\frac{\partial(\rho\Delta H)}{\partial t} \tag{2}$$

$$\Delta H = C_p T + L l_f^{n-1} \tag{3}$$

Here ΔH is the enthalpy due to the solid-liquid phase change; L is the latent heat of solidification; and l_f is the liquid fraction. The laser power melts the metal powder during scanning, and then the molten metal undergoes through solidification process. The amount of heat loss to the surroundings takes place in the form of convection and radiation process are described by Equations 4 and 5 [8]:

$$Q_{conv}^{''} = h(T_\infty - T_s) \tag{4}$$

$$Q_{rad}^{''} = \sigma\epsilon(T_\infty^4 - T_s^4) \tag{5}$$

Here, h is the convection heat transfer co-efficient; T_∞ is the ambient temperature; T_s is the surface temperature; σ is the Boltzmann constant; and ϵ is the surface emissivity. Metal powder is assumed to be fine and spherical shaped in order to neglect the effect of porosity on heat transfer.

2.2.3.2 Structural Analysis.

Due to transient heating and rapid cooling, residual stress develops in the build parts produced in Powder Bed Fusion. Heat transfer occurs through conduction, convection, and radiation process into the build part model and the surrounding environment. Heat transfer due to

solid-liquid phase change is also considered. Residual stress is negligible in the liquid phase. The relationship between elastic stress and strain for an isotropic material is found by using Hooks law described in Equation 6 [5, 6, 8]:

$$\{\sigma\} = [D]\{\varepsilon^e\} \tag{6}$$

Here $\{\sigma\}$ is Cauchy stress; [D] is stiffness matrix and $\{\varepsilon^e\}$ is the elastic strain vector. The total strain $\{\varepsilon\}$ is composed of elastic strain $\{\varepsilon^e\}$, plastic strain $\{\varepsilon^p\}$, and thermal strain $\{\varepsilon^{th}\}$ as presented in Equation 7 [5, 6]:

$$\{\varepsilon\} = \{\varepsilon^e\} + \{\varepsilon^p\} + \{\varepsilon^{th}\} \tag{7}$$

The thermal gradient determines the mechanical response. In the build part model, plastic strain is neglected and does not have any significant effect on the temperature field [5]. The thermal strain $\{\varepsilon^{th}\}$ is calculated by using the Equation 8 [5, 6, 8]:

$$\varepsilon^{th} = \int_{T_{ref}}^{T} \alpha_e(T) dT \tag{8}$$

In this equation, α_e is a temperature-dependent thermal expansion coefficient. The residual stress developed in the build part is calculated from the thermal gradient by using the stress-strain relationship for an isotropic material with linear elastic behavior using the Hook's law [15]. The equivalent stress or Von-Misses stress is used to describe the overall stress field as presented by Equation 9 [6, 8].

$$\sigma_e = \frac{1}{\sqrt{2}} \sqrt{\left(\sigma_x - \sigma_y\right)^2 + \left(\sigma_y - \sigma_z\right)^2 + (\sigma_z - \sigma_x)^2} \tag{9}$$

Where σ_x, σ_y, and σ_z are the x, y, and z components of stress.

2.2.4 Microstructure of Metal Printed Parts

Another drawback of the LPBF process is the development of unidirectional microstructures in the build part that are responsible for the brittleness properties. These columnar grains are developed due to the rapid solidification of the melt pool at each layer. Besides, a shallow melt pool is more prone to rapid solidification, which may give birth to delamination problems. Usually, metal solidification takes place at the bottom and the outer periphery of the melt pool due to direct contact with the surrounding regions. As these regions are cooler than the melt pool, nucleation starts from numerous points and thus leads to grow columnar grains in the build direction. In addition, the columnar grains at the top portion of the melt-pool, get re-melted during fusing with the next layer leading to the development of smaller grains in the corresponding regions. The comparatively slow cooling rate governs the development of equiaxed grains in the middle regions of the melt-pool. These equiaxed grains restore the ductility property, and the columnar grain is responsible for attributing the brittleness properties to the build part. In order to increase the number of equiaxed grains, the temperature of the melt pool should be high enough to inhibit the rapid solidification, in addition the thermal gradient should be low to reduce the heat loss rate. The part's microstructure that develops during the solidification of the melt pool dictates on its mechanical performance [2, 16]. Several studies were conducted on predicting and investigating the grain structures of LPBF manufactured parts. Koepf et al. (2018) [17] developed a cellular automata model to simulate and generate virtual grain structure for LPBF technology. Todaro et al. (2017) [14] discovered that external effects such as the ultrasound decrease thermal gradient and improve the microstructure of the build part. As both the microstructure and the residual stress of the build part depend on the thermal gradient, investigations are being conducted to improve them by optimizing the scan pattern and other input parameters. Akram et al. (2018)

[18] focused on the effect of the scan pattern on the grain structure and reported that a crosshatch scan pattern improves the microstructure of the part. Kudzal et al. (2017) [9] builds a tensile specimen by using six different types of scan patterns. The authors summarize that the hexagonal pattern improves the ductility property of the build part, while the scan pattern with scanning passes oriented along the applied tensile loading direction increases the tensile strength, and perpendicular scanning passes decrease the tensile strength.

2.2.5 Scan Patterns

In LPBF the smaller melt-pool generated for the application of tiny heat source fuses the metal powders through traveling inside the printing contour and fills up the bulk material by following the predefined path denoted as the scan pattern. Thermal gradient and residual stresses are greatly dependent on it. Numerous studies were conducted to characterize the scan patterns and exploring their effect on the build part [3-6, 8, 9]. Qian Chen et al. (2020) [4] developed a continuous scanning path optimization method by using a novel strategy they call "ALSA" (Adaptive Level Set Adjustment) to reduce the residual stress of the build part. Patcharapit et al. (2020) [5] reported that shorter scanning length and optimal energy input reduces thermal gradient and residual stress. Changpeng et al. (2019) [6] discovered that the residual stress is reduced by applying overlaps factor of 25% ~ 50% among the islands. Brandon et al. (2018) [7] observed that scanning strategy influences residual stress. The authors figured out that an edge-to-edge scanning strategy exhibits lower residual stress than a perimeter-first scanning strategy. Jia Song et al. (2018) [3] finds that the rotation strategy of scanning path at each layer also reduces the residual stress. In addition, the amount of residual stress developed for a certain scan pattern varies for different scanning directions. Sezer et al. (2020) [8] found that the thermal gradient changes for a rectangular, concentric scanning strategy through changing the scanning direction (i.e., from center

to edge versus edge to center). The author reported that the higher corner temperatures could be attributed to the change in scanning direction. Sun et al. (2019) [6] developed a novel S-pattern and found that the proposed pattern could reduce residual stress by evenly distributing the heat. The authors reported that the residual stress at the edges or outer portion of the part is higher due to rapid cooling. Kruth et al. (2006) [19] reported that post-scanning with 50% energy reduces residual stress by up to 30%, while Shiomi et al. (2004) [20] found that the rescanning operation with 150% energy reduces residual stress by 55%. Few existing scan patterns are depicted in Figure 4.

(a) Island Zigzag   (b) Regular Zigzag   (c) Spiral Out-center
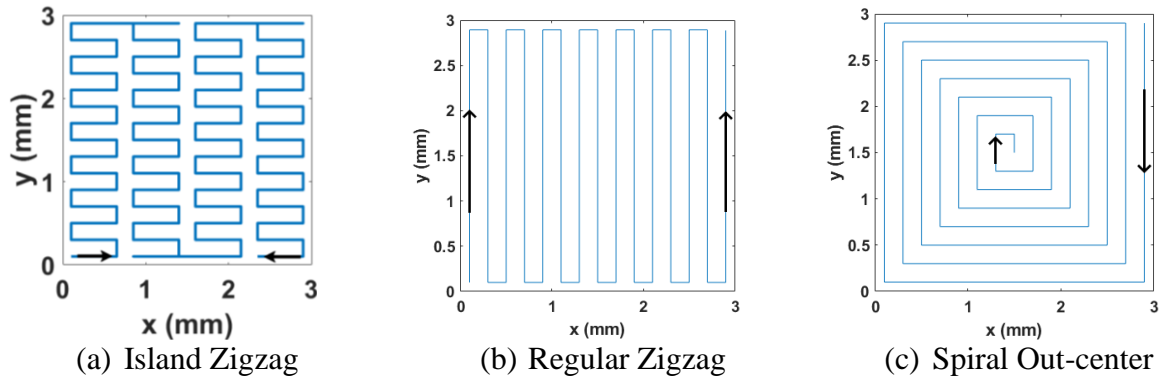
Figure 4: Existing Scan Patterns.

In this thesis, a novel scan pattern is introduced that focuses both on uniform thermal distribution strategy and reheating strategy to reduce the thermal gradient. The corresponding residual stress of the proposed pattern is calculated through using Finite Volume Method (FVM) and compared with other existing scan patterns.

2.2.6 Finite Element Analysis

It can be concluded from the above discussions that, developing an optimum scan pattern is a challenging job and investigating the corresponding mechanical characteristics involves higher cost of equipment and materials. Nowadays, the Finite Element Analysis (FEA) strategy is adopted

to predict the effect of scan pattern on corresponding residual stress, warpage, and other defects [3, 5-8]. The Computational Fluid Dynamics (CFD) analysis is used to investigate the characteristics of the melt-pool which helps to understand the build part quality, and to calculate the temperature of the melt pool. These data are used to calculate the residual stress by using FEA strategy. The FEA is executed in two stages, i.e., 1) Using transient thermal analysis to calculate the thermal history for a pre-defined scan pattern and 2) Calculating the residual stress by importing this thermal history in transient structural analysis [2]. The total strain is calculated from the elastic, plastic, and thermal strain [6]. The inherent strain method calculates the elastic and plastic strain [4]. The total strain is used to calculate the equivalent stress.

2.3 Infill Patterns in Fused Deposition Modeling

The Fused Deposition Modeling (FDM) or material extrusion AM is ubiquitous due to its ease of use and wide applications of plastic components. In FDM, the plastic material is melted and deposited in layer-by-layer fashion through a nozzle using the layer information from the CAD model. Despite its wide applications, the build part contains flaws such as cracks, warpage, surface roughness [21, 22], and poor mechanical performance [23]. The material type and input process parameters such as bed and nozzle temperatures, infill pattern, infill density, layer thickness [24, 25] all influence the quality and mechanical performance of the build part. Furthermore, the desired properties and quality of a part are heavily dependent on its engineering application, making it difficult for designers to select the optimal process parameters. Process planning through Geometric Analysis [26, 27], numerical approach through Finite Element Analysis (FEA) [28], experimental investigation [29, 30], data driven modeling with machine learning [31], and other studies have been conducted to address this issue in various ways.

16

The strategy of adding material in layer-by-layer manner broadens the scope of producing lightweight parts through replacing the bulk material with infill lattice inside the skin of the build part. The rigidity of the build part is dictated by the type of infill lattice used, infill density, layer adhesion, and the material used [32]. Furthermore, the build part exhibits higher mechanical strength (compressive and tensile) for applied loading along the raster direction compared to the other directions [33]. Yao et al. (2019) [34] discovered that the tensile strength increases with increasing raster angle from 0° to 90° and decreases with increasing layer thickness. Infill Pattern (IP) describes the orientation of the raster and thus the strength of the build part. Aloyaydi et al. (2020) [33] performed LVI and compression tests on PLA printed parts for four different IPs: triangle, grid, quarter cubic, and tri-hexagon. The authors discovered that the triangle IP had the highest peak load and penetrating energy. Fernandez-Vicente et al. (2016) [32] discovered that honeycomb IP has a higher tensile strength than rectilinear IP. Ahsan et al. (2021) [23] innovates a novel continuous toolpath strategy for honeycomb infill pattern. Figure 5 depicts few common infill patterns available in commercial slicing software.
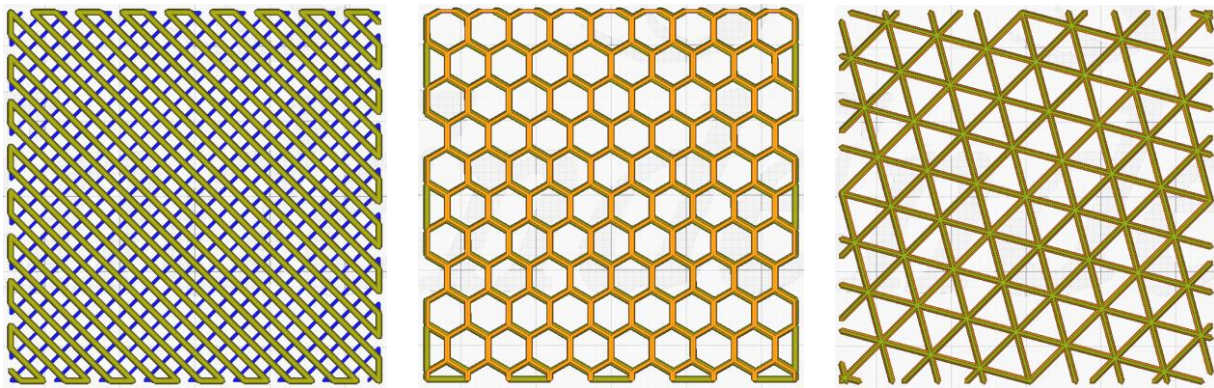
(a) Zigzag　　　　　　　　(b) Honeycomb　　　　　　　　(c) Triangle

Figure 5: Existing Infill Patterns (Prepared by using Ultimaker Cura 4.10.0)

In this thesis, a novel hybrid infill pattern is developed through combining the regular Zigzag and Honeycomb patterns to restore the advantage of the simple toolpath of the Zigzag pattern and the better mechanical performance of the Honeycomb pattern. The proposed pattern is island type that reduces the unidirectional raster length compared to the Zigzag pattern and restores the weaving nature through 90º layer rotation; thus, it distributes the strength along both perpendicular directions of a 2D plane. A mathematical model for the proposed infill pattern is established, as well as the effect of infill parameters on relative infill density. This model offers the scope of tailoring the porous infill structure and density by controlling the infill parameters. Compression tests are executed to characterize the mechanical properties of the proposed infill pattern, which are then compared with the other existing infill pattern.

CHAPTER THREE: DEVELOPING SCAN PATTERNS FOR LPBF AM PROCESSES

3.1 Chapter Introduction

Residual stress greatly depends on the thermal gradient over the build part which can be reduced by increasing the surroundings temperature and uniformly distributing the thermal energy. In this chapter a novel scan pattern is developed based on uniform thermal distribution and reheating strategy. The residual stress is calculated by using Finite Volume Method (FVM) for the proposed scan pattern and compared with other existing scan patterns such as Zigzag, Island Zigzag and Spiral scan patterns.

3.2 Developing Scan Pattern

The scan pattern has a significant impact on the thermal gradient, and a good scan pattern should have the following properties [6]:

1. A minimal number of start-stop times for the laser beam during the scanning of a single layer since this allows more time to localize heat. Ideally, the scan pattern should be continuous [35].

2. A low number of scanning turns as it allocate/localize thermal distribution at the turning points or corners [8].

3. Allowance to generate a weave pattern. The weave that is generated due to the 90° rotation of scan patterns at each layer is beneficial for the build part strength [36].

4. A short scanning length that allows for an island scanning strategy since this raises the temperature at each island and prevents rapid solidification of melt-pool [5].

Based on the above principles, a novel scan pattern is developed and described in section 3.2.1. It is noted that a controlled compressive residual stress is beneficial due to its effect on increasing

fatigue strength, resistance to stress corrosion cracking, and slow crack propagation. Conversely, tensile residual stress is detrimental to the build part as it reduces fatigue strength and induces stress corrosion cracking. As the tensile residual stress originated from non-uniform thermal distribution, the proposed scan pattern focuses on uniform thermal distribution and reheating strategy to alleviate the tensile residual stress.

3.2.1 Alternating Double Pass Spiral Scan Patterns

The alternating double pass spiral scan pattern is a novel scan pattern with a continuous laser track i.e. no internal start-stop point for the laser beam in a layer. In the proposed scan pattern, the laser beam starts tracking through the blue colored lines in a spiral manner, from the outside corner to the center named as forward pass and then returns to the same corner through traversing the red colored lines denoted as returning pass as shown in Figure 6.
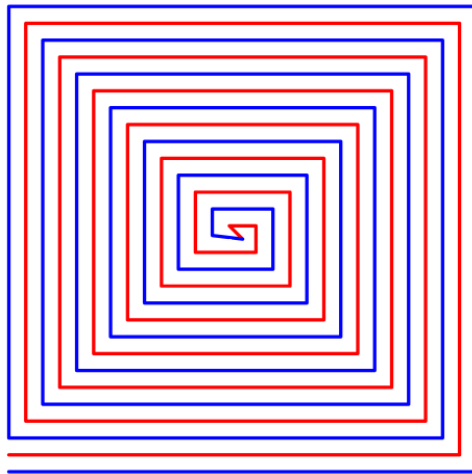

Figure 6: Proposed alternating spiral scan pattern.

This pattern contains very few turning points compared to the several existing scan patterns such as island type zigzag scan pattern. These turning points of the laser track are responsible for higher temperature at the corners [8] due to the turning of scanning direction by 90° localizes the thermal

energy toward both the transverse and longitudinal direction of that corner point perpendicular to the build direction. Although the proposed scan pattern lacks the weaving properties for a square strip, it allocates the scanning passes towards both the transverse and longitudinal direction of the printing plane at each layer. This strategy distributes the thermal energy and thus the development of inherent stresses along both directions. One of the drawbacks of the proposed pattern is the long scanning length as this allows the rapid solidification of melt pool, which is responsible for developing residual stress. To compensate this effect, the residual stress developed during the forward passes are alleviated through the re-heating action of the returning passes [Figure 7]. In addition, the residual stress developed in the returning passes may get reduced due to the reheating action of the next layer.

On the other hand, the changes in scanning direction influence the thermal history and residual stress. The effect of changing the scanning direction, such as edge-center-edge and center-edge-center, for the proposed scan pattern on the thermal gradient and residual stress of the build part can be a topic for future study [Figure 7].
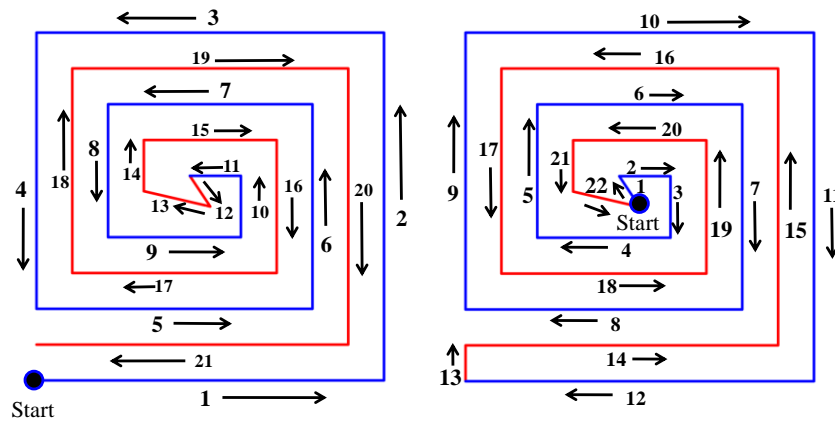

Figure 7: Alternating Double Pass Spiral Scan Pattern from center to edge to center (Right) and from edge to center to edge (Left).

Figure 7 represents the blue lines as forward pass and red lines as returning pass for both scanning directions. The number of alternating lines (blue or red) from the center to edge at each direction can be obtained from Equations 10 and 11.

$$n_{L_x} = \frac{L_x - D_L}{4D_L} + 1 \tag{10}$$

$$n_{L_y} = \frac{L_y - D_L}{4D_L} + 1 \tag{11}$$

Where L_x and L_y are the strip length along x and y axes, and D_L is the laser beam diameter. Furthermore, as the scan pattern describes the alternating passes scanning strategy, there is possibility of having scan gaps or un-melted regions between the intersections of forward and return scanning passes due to the shrinkage of metal solidification during the forward pass. To resolve this issue, overlapping among the successive scanning passes along the scanning direction can be included as described by $hatch\ spacing = Overlap\ factor \times D_L$. Where the value of the overlap factor is less than 1 and its effects on residual stress can also be a topic for future study.

3.2.2 Existing Scan Patterns Considered in this Study

Two groups of scan patterns are investigated in this study namely the zigzag group and the spiral group. It was observed in earlier studies that the frequent start-stop of laser beam in a single layer influences heat localization [35]. Although the Island Zigzag scan pattern depicted in Figure 8(b) exhibits several start-stop conditions of the laser beam, the selected scanning directions reduces the time in between, thus reduces the heat localization. On the other hand, the scanning direction for the spiral group scan pattern is selected from outside/edge to center. Although the proposed scanning directions exhibited heat localization at the center [8], this scanning direction is selected for this study to compare the tendency of heat localization at center for the proposed novel scan pattern with the existing spiral scan pattern. In the island type scan pattern, the scanning

direction is selected such that the laser beam stopping time can be minimized at each layer to
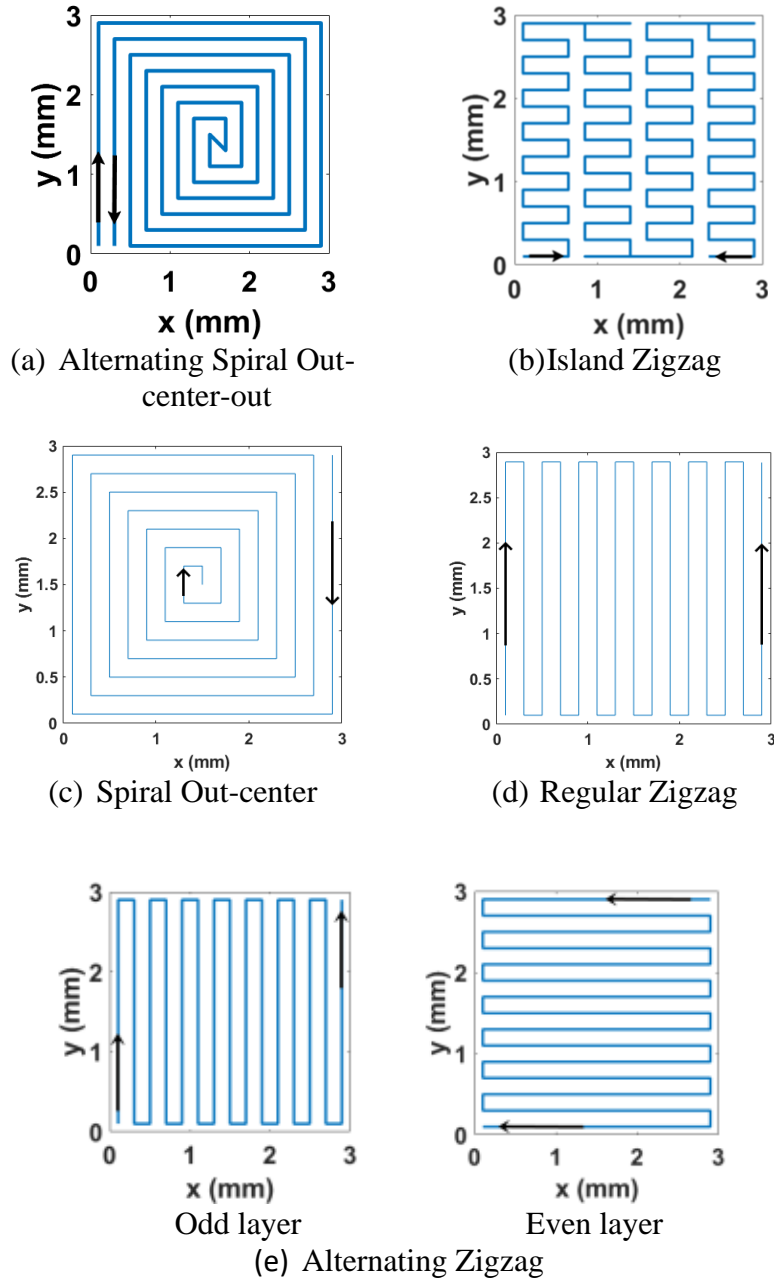reduce the thermal gradient induced from it.

(a) Alternating Spiral Out-center-out

(b) Island Zigzag

(c) Spiral Out-center

(d) Regular Zigzag

Odd layer   Even layer
(e) Alternating Zigzag

Figure 8: Scanning Direction of the Scan pattern.

3.3 Numerical Finite Volume Method (FVM)

In this thesis, a numerical approach is used to predict the residual stress on the build part for the scan patterns depicted in Figure 8 based on the mathematical model described in section 2.2.3. A finite volume toolbox of MATLAB is used to develop the model [37]. FVM is based on mass, momentum, and energy conservation and is more convenient to implement the solidification phase change process induced with complex boundary conditions involved in the LPBF processes. In addition, FVM strategy reduces the computational load and can produce highly accurate results in a reasonable amount of time. However, accuracy is affected by the meshing size, time step, and other factors.

A 3mm X 3mm computational domain with 4 scanning layers is considered for the numerical simulation in this study. The bottom surface is considered as a fixed temperature boundary condition with conduction heat transfer, and the top and the side surfaces are considered for convection and radiation heat transfer. Conduction heat transfer is considered for the powder bed and solid portion of the build part. Here SS316L material is selected for the simulation [8]. The input process parameters used in this study (Table 1) are adopted from previous studies [38, 39] based on the EOS M290 machine.

Table 1: Process parameters adopted from previous studies [38, 39].

| Laser Beam Diameter	$D_L = 0.2\ mm$	Laser Power	45.7 W
Layer Thickness	$\delta = 30\ \mu m$	Scan Speed	1.2 m/s
Mesh Size along XY plane	$\dfrac{D_L}{8}$	Pre-heating Temperature	80ºC
Mesh Size along Build Direction	$\dfrac{\delta}{2}$	Laser Inactivation Time	6 s

3.4 Results and Discussion

The whole study is divided into two chapters to explain the effect of material deposition strategy on two different categories of AM technology i.e. the residual stress development for different scan patterns in the LPBF printed parts and the mechanical behavior of different infill patterns in the FDM printed parts.

### 3.4.1 Thermal History and Residual Stress in LPBF additive manufacturing process

The LPBF process generates compressive residual stress during the solidification of the melt-pool. The melt-pool formed by the interaction of the laser beam with metal powder is so small that it solidifies quickly right after the laser beam passes the melted region. During this rapid solidification, the metal shrinks and exerts a mechanical force on the surrounding area, causing compressive residual stress in the build-part. On the other hand, the moving heat source causes transient heating at different portions of the build part causes un-even thermal expansion which results tensile residual stress. Hence, the residual stress is heavily influenced by the melt-pool temperature and the thermal gradient of the build part. Figure 9 depicts the thermal histories produced by the scan patterns shown in Figure 8. The scan patterns used in this study is divided into two groups i.e. the Zigzag group and the Spiral group to compare and discuss their effects.

In the zigzag strategy group, the regular Zigzag, Alternating Zigzag, and Alternating Island Zigzag scan patterns (shown in Figure 8 (c, d, e)) are discussed. The regular Zigzag scan pattern consists of a series of bi-directional scanning lines. In these patterns the scanning passes are oriented parallel and tend to localize the heat energy in a certain portion of the build part during scanning. Moreover, the temperature at both ends of the scanning passes are higher than the temperatures of the rest of the strip due to the heat localization at all turning points [8], and these turning points are located along the edges of the computational domain. The peaks of temperatures
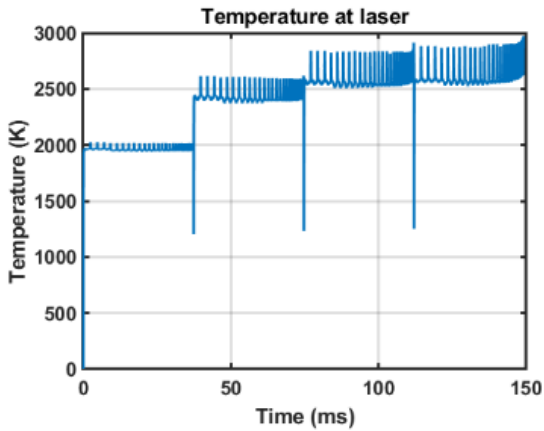
25

shown in Figure 9(a) represent the turning points, results higher tensile stress values along edges (Figure 10(b)).
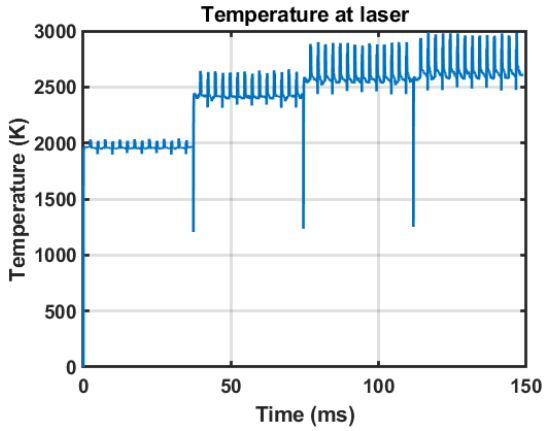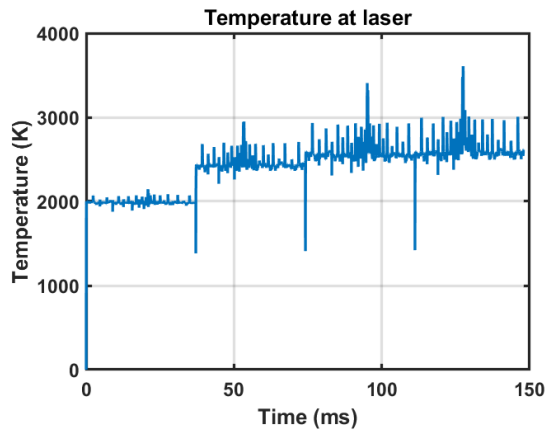

(a) Regular Zigzag pattern temperature
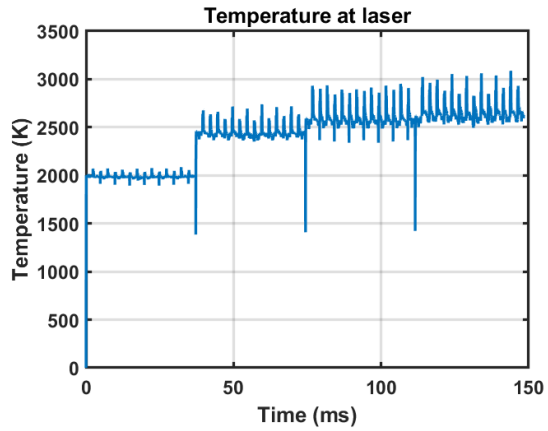
(b) Alternating Zigzag pattern temperature

(c) Spiral Out-center pattern temperature

(d) Alternating Double Pass Spiral pattern temperature
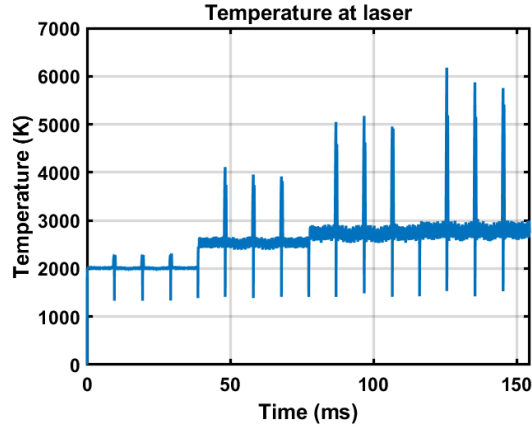
(e) Alternating Island Zigzag pattern temperature

Figure 9: Thermal Gradient of the scan patterns

Thermal gradient is generated from the edges to the center of the body due to the higher temperature difference. The tensile residual stress at the strip's edges is higher, as rapid cooling of the midsections causes shrinkage and exerts pulling force along edges. Furthermore, the layer wise tensile stress value fluctuates around a constant value, and it decreases in successive layers due to the re-heating effect of the previous layer, that inhibits rapid solidification. Figure 10 depicts that the maximum tensile residual stress at the first layer of the regular zigzag scan pattern is greater than 650 MPa.
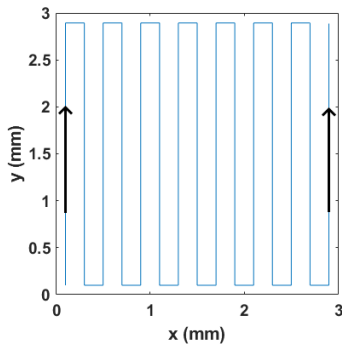
(a) Scan pattern
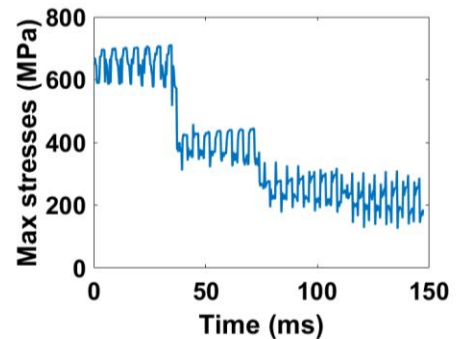
(b) Max stress vs. time
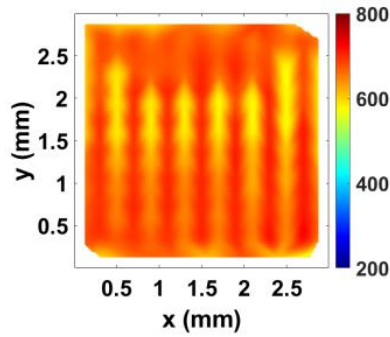
(c) Layer 1 max stress

(d) Layer 2 max stress

(e) Layer 3 max stress

(f) Layer 4 max stress

Figure 10: Max thermal stresses [MPa] for regular Zigzag pattern.

Figures 10(c, d, e, f) and 11(c, d, e, f) presents residual stress simulation results for regular and Alternating Zigzag scan patterns, indicating that the corresponding scanning passes are reflected through the inherent stress fields. The fluctuation amplitudes of the top layer tensile stresses (Figures 10(b) and 11(b)) and temperatures (Figure 9(a, b)) are lower for the 90° rotation strategy of the scan patterns at each layer than for the no rotation strategy. It is observed that the tensile residual stress values range from 150MPa to 350MPa for a no rotation (regular zigzag) pattern and from 180MPa to 300MPa for a 90° rotation (alternating) pattern. The pattern rotation strategy at each layer results in such benefits due to more uniform thermal distribution.
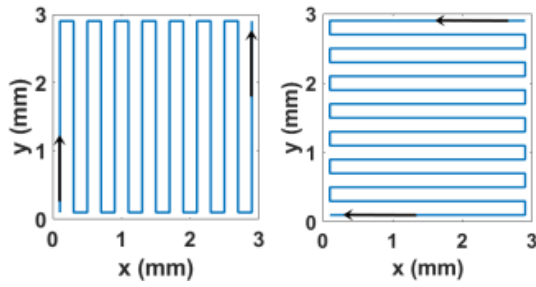
(a) Scan pattern

Layers 1 & 3   Layers 2 & 4

(b) Max stress vs. time
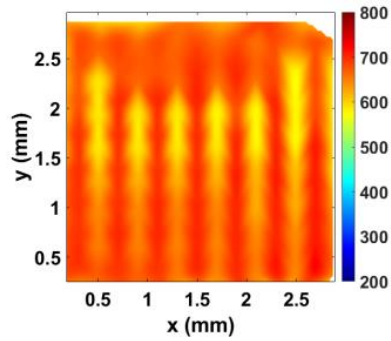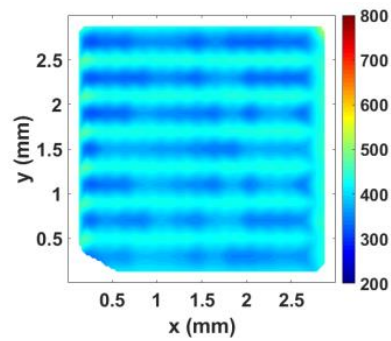
(c) Layer 1 max stress
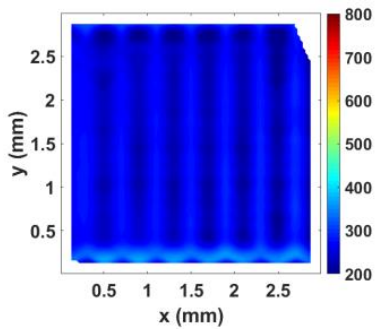
(d) Layer 2 max stress
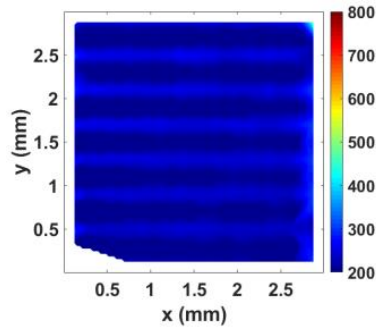
(e) Layer 3 max stress

(f) Layer 4 max stress

Figure 11: Max thermal stresses [MPa] for Alternating Zigzag pattern.

The Alternating Island Zigzag pattern on the other hand, exhibits average tensile residual stress of more than 650 MPa at the first layer. The pattern consists of four individual islands with three interconnections among them. Figure 12(a) depicts the bi-directional scanning strategy of the

islands causes the higher temperatures at the island interconnections' edges. Furthermore, convection heat transfer occurs at the edges accelerating the rapid cooling process. This uneven thermal distribution introduces tensile residual stress.
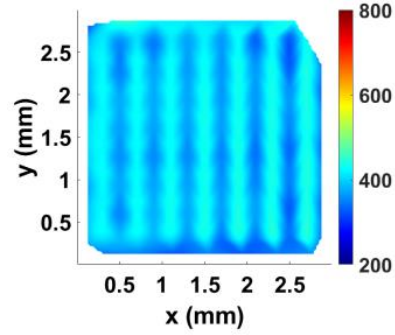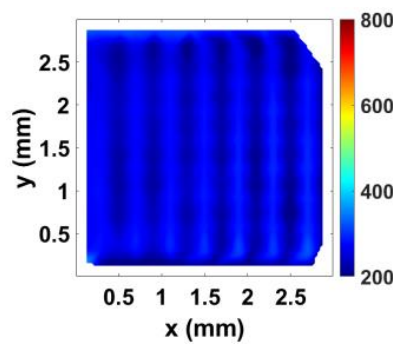

(a) Scan pattern

(b) Max stress vs. time

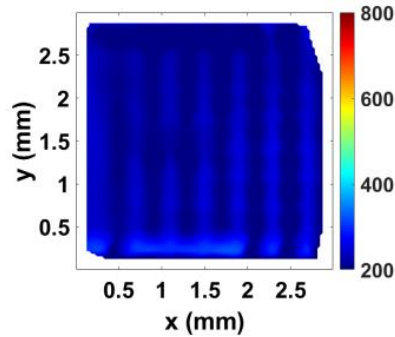(c) Layer 1 max stress

(d) Layer 2 max stress

(e) Layer 3 max stress

(f) Layer 4 max stress
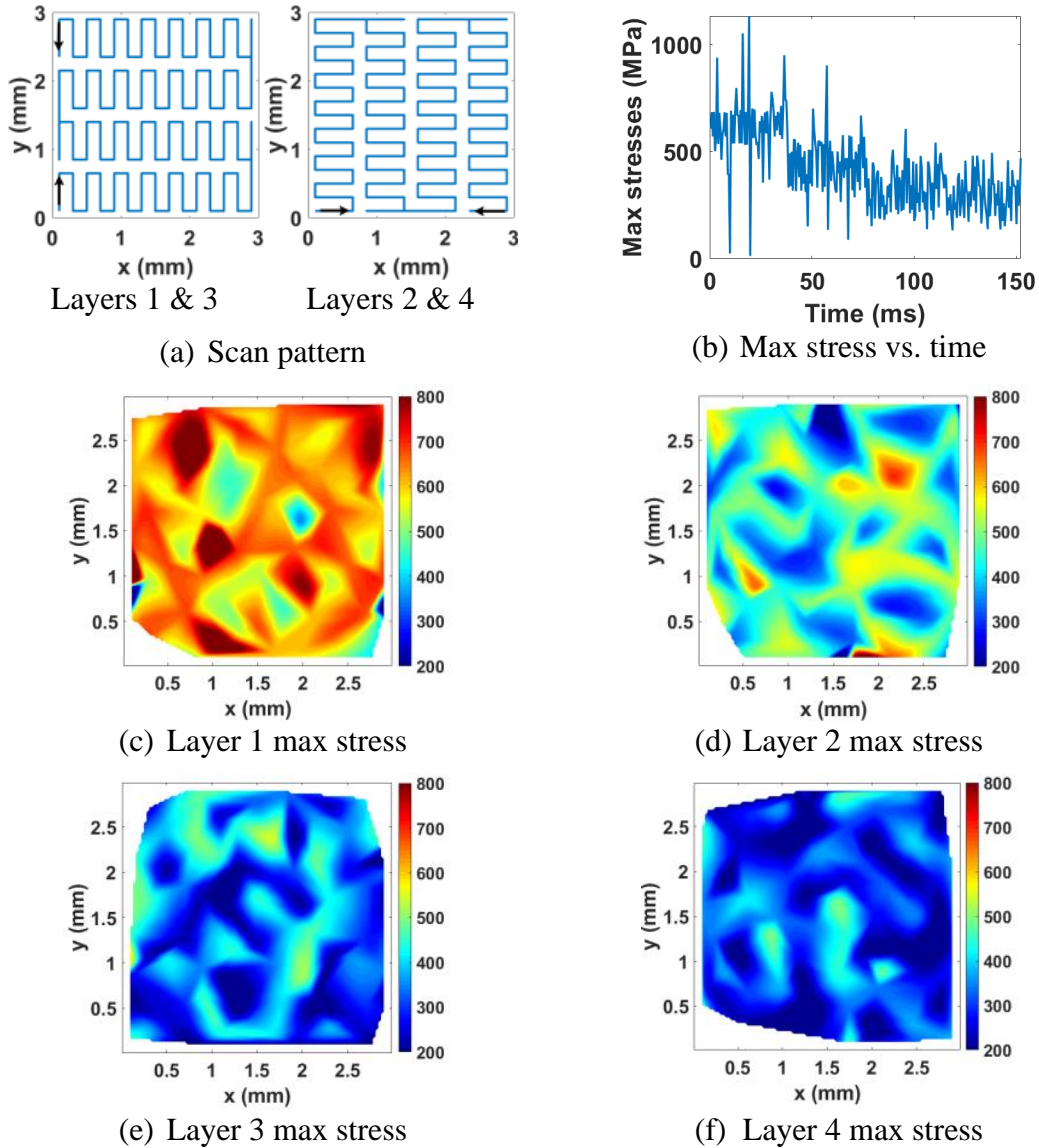
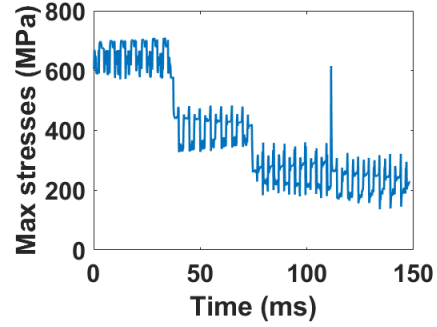Figure 12: Max thermal stresses [MPa] for Alternating Island Zigzag pattern.

Due to the presence of numerous scanning turning points throughout the strip, the Alternating Island Zigzag pattern contains stress spikes across the entire strip at each layer, which is not similar to the regular Zigzag pattern. Although the turning effect of the laser scan causes

30

these spikes, Figure 12(b) shows a few major peaks and valleys at the first layer, which are gradually reduced in subsequent layers. The higher thermal gradient regions cause the peaks of stresses.

Furthermore, the initial and final scanning passes of each even island are scanned twice by laser beam as shown in Figure 12(a). This twice scanning causes peak temperature at those points (Figure 9(e)), resulting in higher thermal gradient and trough stress values as shown in Figure 12(b). According to Figure 13, there are two even islands and a total of three scanning passes (island interconnections) that are scanned twice, resulting in three peak temperature values and three trough stress values.
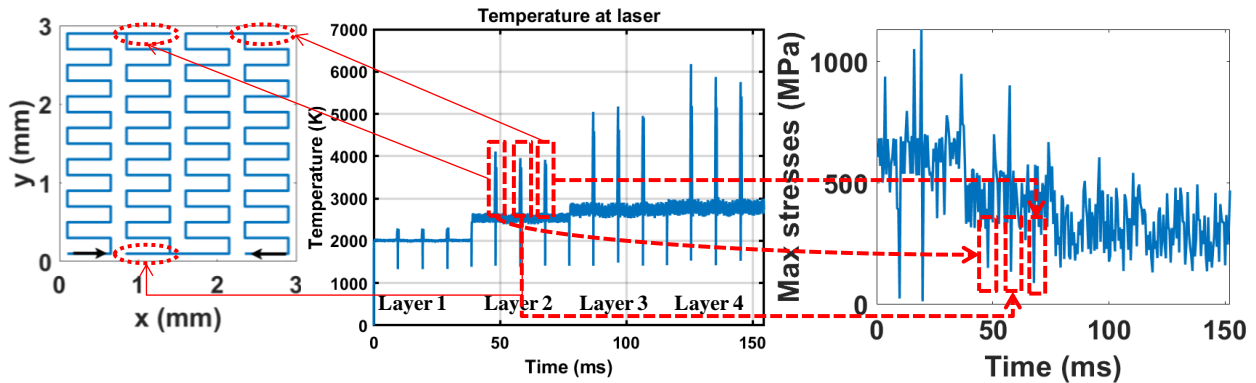
Figure 13: Temperature spikes for alternating island zigzag scan pattern.

The 90° rotation strategy at each layer eliminates the thermal gradient for the Alternating Island Zigzag pattern as each new layer is re-heated by the previous layers. The combined effect reduces the overall tensile residual stress and spikes in successive layers.

In addition, the Alternating Island Zigzag pattern has more turns than the regular Zigzag pattern because of the shorter scanning pass length causing higher surface temperature which should result in lower residual stress. But the residual stresses are nearly the same for both patterns due to the higher thermal gradient. Promoppatum et al. (2020) [5] discovered that scanning lengths

31

less than 5 mm significantly increased the surface temperature, which inhibits rapid solidification and lower residual stress. Although the scanning length in both cases is less than 5 mm, no significant difference in stress values are observed since the island wise scanning strategy localizes the heat along islands and generates higher thermal gradient.

Another pattern group consists of the Spiral out-center scan pattern and the Alternating Double Pass Spiral out-center-out scan pattern. Both patterns have long scanning passes and fewer scanning turns. Figure 9(c) depicts the temperature spikes for the spiral out-of-center scan pattern that corresponds to the corner turning points. The inherent tensile residual stresses are higher in the first layer and decrease with the addition of new layers, resulting in a reduction in overall stress from 700MPa to 300MPa, as shown in Figure 14(b). Although in Spiral pattern, more even thermal distribution is obtained compared to the Zigzag patterns due to the even distribution of scanning passes in both lateral and transverse directions, higher tensile residual stresses are generated into the build part. The longer scanning passes experiences rapid cooling and heat localizes at the center [8] of the strip resulting a thermal gradient along edge to the center and thus develops the tensile residual stress.
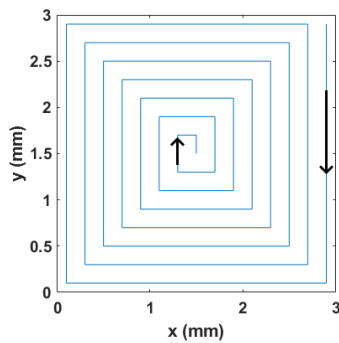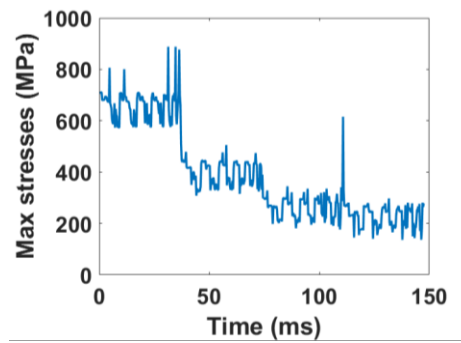
(a) Scan pattern

(b) Max stress vs. time
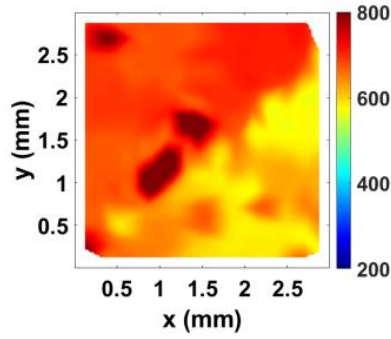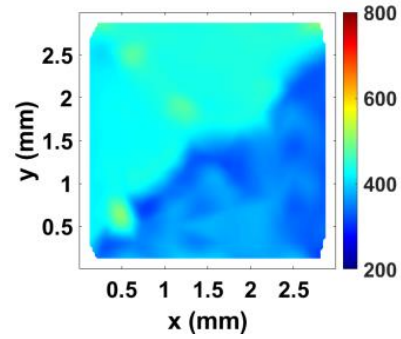
(c) Layer 1 max stress   (d) Layer 2 max stress
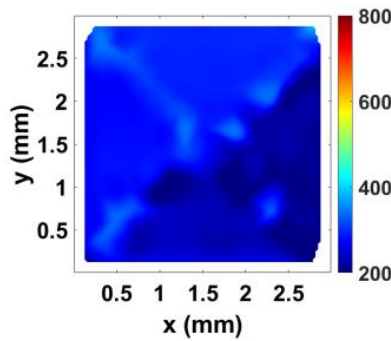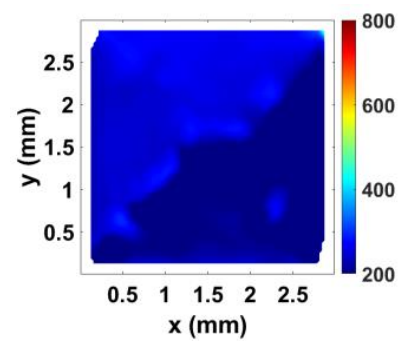
(e) Layer 3 max stress   (f) Layer 4 max stress

Figure 14: Max thermal stresses [MPa] for Spiral out-center scan pattern.

In the Alternating Double Pass Spiral scan pattern, the laser beam scans the forward pass spiral lines first and then returns through the return pass spiral lines as shown in Figure 15. Unlike the other patterns discussed above, the forward pass spiral lines are initially free on both transverse sides before fusing with the returning pass lines during scanning. Temperatures at corner turning points in spiral patterns are higher than at any other point along the corresponding scan passes [8]. Moreover, the scanning lines experience compressive stress along the scanning direction due to the Poisson effect [4]. The combined effect of compressive stress and higher corner temperature raises the tensile residual stress at the corners more than any other points. Figure 15(b) depicts several stress spikes at each layer, which represent the higher tensile stresses at the corners.

33

(a) Scan pattern

(b) Max stress vs. time

(c) Layer 1 max stress)

(d) Layer 2 max stress

(e) Layer 3 max stress

(f) Layer 4 max stress
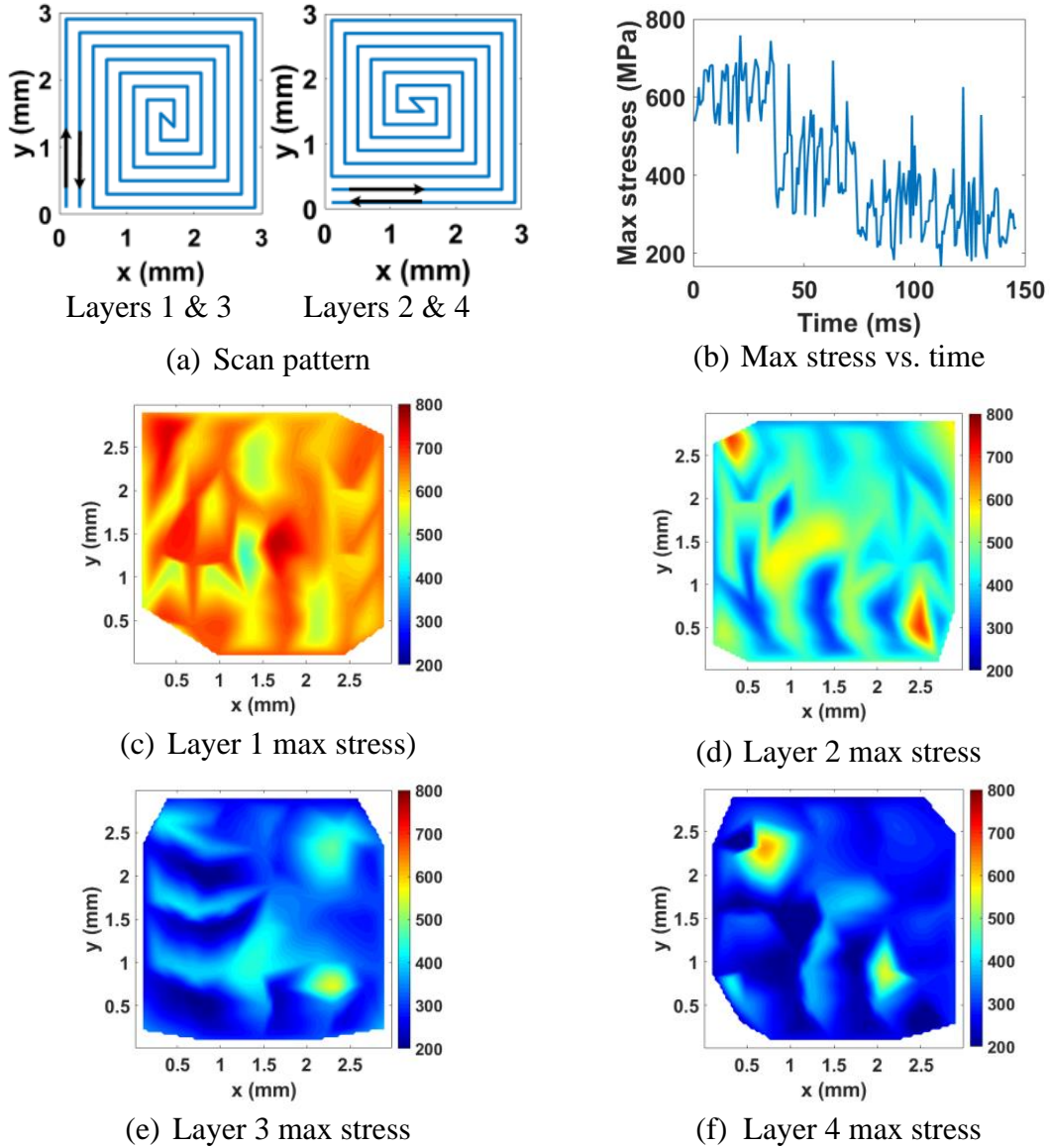
Figure 15: Max thermal stresses [MPa] for Alternating Double Pass Spiral pattern.

Convection heat transfer occurs at the strip's edges, which is also responsible for generating higher thermal gradient and thus the higher tensile residual stress at the border. However, due to the alternating scanning strategy of the double pass spiral pattern, the stress distribution shown in Figure 15(b) differs. During scanning the forward pass, there are some un-melted regions between the parallel scanning passes, which increases the rapid cooling tendency and results in higher thermal gradient and residual stress. The re-heating effect of the return pass scanning reduces the

elevated stresses. Moreover, during the solidification of the returning passes the shrinkage force is exerted on the neighboring forward passes due to the fusion action among them. This intricate interaction between the forward and return passes, results fluctuations of stresses along the build part exhibiting the compressive and tensile stresses. Furthermore, the scanning begins at the outside corner, moves to the center, and then returns to the outside corner. Thus, the temperature of the center increases due to heat accumulation (the temperature peaks shown in Figure 9(d)), during forward pass and then the heat dissipates from the center to the outside. This combined effect localizes heat at the center in forward pass which dissipates outwards during the returning pass and thus it reduces the thermal gradient and overall tensile residual stress of the build part in each layer.

In addition, more even thermal distribution is resulted from the 90° rotation (alternating) of the double pass spiral pattern's scanning strategy, and the re-heating effect of the bottom layers reduces the residual stresses on top layers. This pattern effectively reduces the thermal gradient and residual stress from the first layer, as shown in Figures 9, 10(b), 11(b), 12(b), 14(b), and 15(b). The overall tensile residual stress of the first layer for this pattern is approximately 600 MPa, whereas it ranges from 650 MPa to 700 MPa for other existing scan patterns investigated in this study.

It is noted that the simulation results give only the tensile stress values and no compressive stress values are exhibited (all stress values are positive). The mathematical model used for the numerical analysis considers the development of residual stress based on the thermal gradient of the build part. In addition, the effect of plastics strain component resulting from the thermal gradient is completely ignored and the strain developed due to the thermal load is considered as elastic in nature. According to the Von Misses failure theory, an object undergoes failure while

35

the inherent Von Misses stresses are equal or greater than the tensile yield strength of the material. According to DIN EN ISO 6892-1:2009 the upper yield strength of SS316L is 230.7 MPa. Yan et al. (2012) reported that the yield strength of coarse grain SS316L is 250~300 MPa [40]. Wang et al. (2018) found that the tensile yield strength of SS316L part printed on LPBF process is 450~590 MPa [41], which indicates that the plastic deformation should take place during scanning for all scan patterns discussed. This plastic deformation would alleviate the total residual stress amount that is obtained from the simulation result and may provide a more real approximation of the tensile and compressive components of the residual stress. In order to incorporate the plastic strain into the mathematical model, it is required to develop and include the elasto-plastic constitutive model to the existing model.

Since the computational model calculates all inherent stresses for an isotropic material with linear elastic behavior, the approximated stress values are higher as it restores the stress values against the plastic strain. Due to the limited accessibility of the available EOS M290 LPBF printer, it is difficult to experimentally validate the residual stress data for the customized scan patterns. However, the simulation results are within a certain range of other studies despite some differences in input parameter values.

Smith et al. (2021) found that the tensile residual stress of LPBF printed part was around 411±15 MPa measured through Neutron Diffraction testing [42]. The authors used laser power of 250W, scan speed 278 mm/s, and laser beam diameter of 80µm. The size of the rectangular specimen was 20 mm X 10 mm X 10 mm and customized the Zigzag scan pattern was used. The authors discovered that the bottom layer experiences tensile residual stress of 411 MPa and the top layer exhibits compressive residual stress of -285 MPa. Williams et al. (2020) found tensile residual stress of 450 MPa in FEA analysis performed through ABAQUS and principal stress

component values within a range of 100~350 MPa were found through XRD testing [43]. The

authors used a 200W laser, and a laser beam diameter of 65µm in the experimental LPBF system.

The size of the computational domain was 0.3 mm X 0.3 mm X 0.26 mm in ABAQUS and Zigzag

scan pattern was used with 67° rotation at each layer. Both experiments discussed above used

SS316L metal powder for their experiment. It can be concluded from the existing study that the

predicted residual stress amount is higher (around ~200 MPa) than the experimental findings

despite the differences in input parameters. It is optimistic that the developed simulation model

used in this research can approximate a more accurate solution if the plastic strain component is

accounted for through incorporating the elasto-plastic constitutive model with it.

3.5 Chapter Conclusion

The effects of four scan patterns, as well as the novel pattern, on the build part thermal

history and residual stress are investigated in this study. The thermal history for the layer-by-layer

LPBF process is numerically calculated using the Finite Volume method, and the equivalent

residual stresses (Von-Misses stress) are evaluated using the resulting thermal gradient. This study

also investigates the effect of 90° rotation of the scan patterns at each layer on the resulting thermal

gradient and residual stress.

It can be concluded from this study that the alternating zigzag pattern has lower overall

residual stress than the regular zigzag pattern. Besides, the higher surface temperature of the build

part for alternating island zigzag pattern prevents rapid solidification. Furthermore, the application

of 90° rotating scanning strategy at each layer results in a reduction of the thermal gradient, with

the exception of a few temperature/stress spikes caused by the scanning direction. On the other

hand, the novel alternating double pass spiral pattern distributes heat over the entire build part in

the forward pass and reheats the entire region in the return pass. Although this scanning strategy produces some temperature spikes, it does reduce the tensile residual stress from the first layer.

Future research can be carried out by varying the scanning direction of the scan patterns. Through an introduction of overlap between each scanning pass, the proposed novel scan pattern can be studied further. To measure the residual stress of the build part and validate the findings of this study, an experimental study with non-destructive testing needs to be performed.

CHAPTER FOUR: DEVELOPING AND CHARACTERIZING INFILL PATTERN FOR FDM PROCESS

4.1 Chapter Introduction

Aside from the printing parameters such as nozzle temperature, bed temperature, printing speed, and extrusion rate, the infill pattern plays a key role in the mechanical performance of the printed object. In this chapter, a novel infill pattern is developed, and its mechanical performance is evaluated. The proposed pattern is island type which combines the regular Zigzag and Honeycomb infill pattern to restore the benefits of both infill pattern such as manufacturing simplicity of Zigzag infill pattern and better mechanical attributes of Honeycomb infill pattern. The mechanical behavior of the proposed pattern is explored through compression test and compared with the Zigzag infill pattern.

4.2 Modeling Infill Pattern for FDM

The proposed infill pattern is zigzag in nature with repeating hexagonal shaped lattice cells. The subsequent arrangement of these cells in a row develops the island. The zigzag nature provides the scope of generating continuous toolpath in the island as depicted in Figure 16.

a. Patterns at odd layer
(90° rotation)

b. Patterns at even layer
(no rotation)

c. Top view of the Proposed
infill pattern
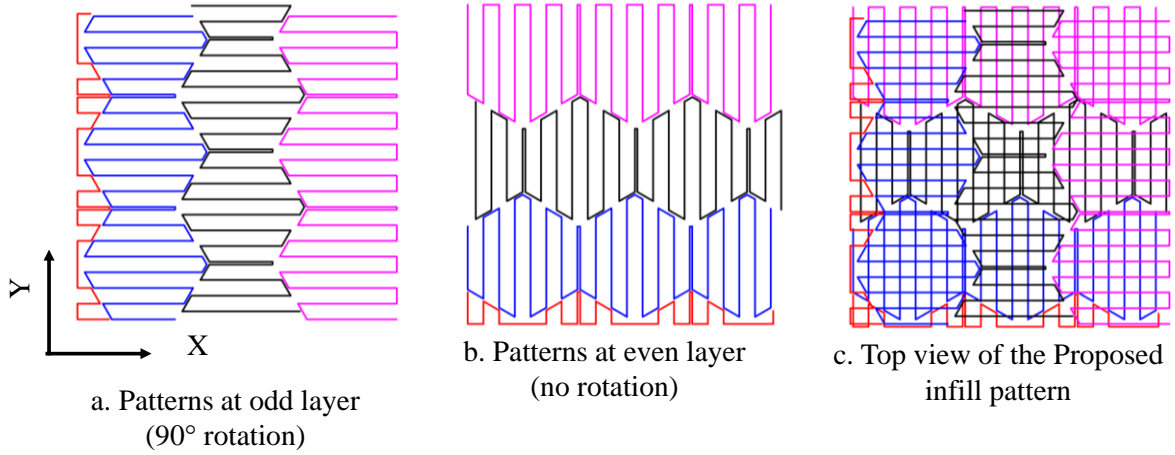
Figure 16: Proposed Infill Pattern

4.2.1 Unit Hexagonal Cell

Each island depicted in Figure 17 is a repeating arrangement of the unit cell. The unit cell is formed by a group of parallel zigzag raster with variable lengths that are equally spaced and oriented in a manner to reflect the hexagonal shape.

The size of the hexagon in the proposed pattern can be determined by the total number of zigzag raster, n_r, and the hatch space, h_s. Equation 12 expresses the arm length, L_a, of the proposed regular hexagon unit cell in terms of n_r and h_s.

$$L_a = \frac{(n_r - 1)(h_s + d_n)}{2 \cos 30°} \tag{12}$$

where d_n is the raster width (filament diameter). The proposed model considers even integer values for n_r in order to facilitate the repeating unit cells with same starting points as shown in Figure 16.
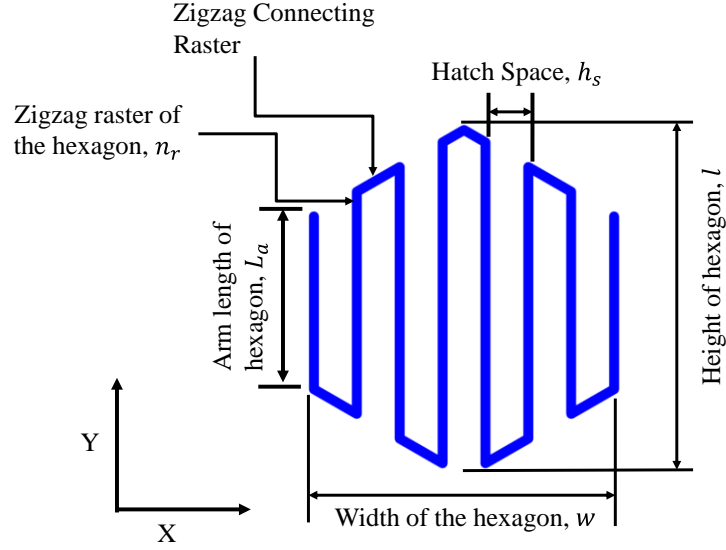
Figure 17: Unit hexagonal cell of the proposed pattern.

Equations 13 and 14 express the width, w, and height, l of the hexagon unit cell, respectively.

$$w = 2L_a \cos 30° \tag{13}$$

$$l = L_a + 2L_a \sin 30° \tag{14}$$

The length, l, and width, w, of a hexagon define its size. Both size parameters for a regular hexagon are determined by using the arm length L_a (Equations 13, 14), i.e. the infill parameters namely the zigzag raster number, n_r, raster width d_n, and hatch space, h_s. (Equation 12).

4.2.2: Relative Infill Density

The relative infill density and the type of infill influence the strength of the build part. The amount of material used to construct a porous unit cell compared to the unit cell's solid counterpart describes the infill relative density. It can also be expressed as the ratio of the material volume in a porous unit cell (V_p) to the volume of a solid unit cell (V_s). Equations 16 and 17 can be used to calculate and material volume, V_p, of the porous unit cell and the volume of the solid hexagon unit

cell, V_s. For the sake of simplicity, a raster shape with a circular cross-section is considered. Equation 18 determines the relative infill density, D.

$$R_l = n_r L_a + \frac{h_s}{2\sqrt{3}}(n_r{}^2 + 2n_r - 4) \tag{15}$$

$$V_p = \frac{\pi d_n{}^2}{4} R_l \tag{16}$$

$$V_s = \frac{3\sqrt{3}}{2} a^2 d_n \tag{17}$$

$$D(\%) = \frac{V_p}{V_s} \times 100 \tag{18}$$

Here, R_l is the total length of the raster in a unit cell.

4.2.3 Toolpath Design

Designing a continuous tool path for a hexagonal infill pattern capable of printing all six sides/arms of each hexagon cells in a single layer is challenging [23]. Due to the zigzag nature of the proposed pattern, it facilitates creating a continuous tool path for each hexagon in an island. Figure 18 depicts that the longitudinal axis (or X axis for even layers) consists of the periodic arrangement of hexagonal unit cells, denoted as islands. These islands are parallel oriented along transverse axis and fills the printing contour. Equation 19 describes the number of islands, $\lfloor m \rfloor$, for a rectangular block and it depends on the size of the unit cell.

$$\lfloor m \rfloor = \frac{y - d_n - L_a \sin 30°}{L_a + d_n + L_a \sin 30°} \tag{19}$$

Here, the length and width of rectangular block is defined by x and y respectively and $\lfloor m \rfloor$ represents the integer floor value of m. The fractional value calculated from Equation 19 represents the $(\lfloor m \rfloor + 1)^{th}$ island consisting of fractional unit cells.
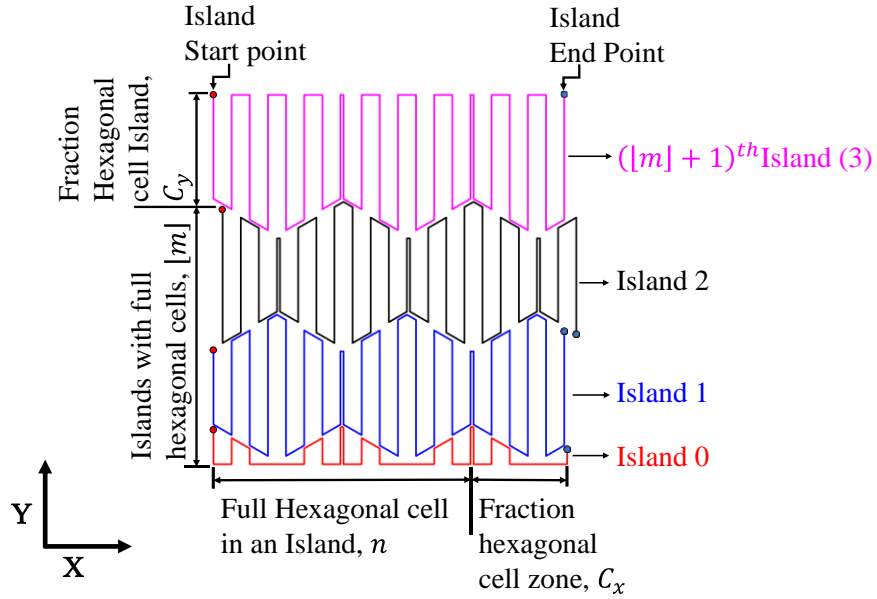
Figure 18: Description of the proposed infill pattern

The purpose of "Island 0" is to fill the empty space beneath "Island 1" as shown in Figure 18. For this reason, it is not considered as an island. To ensure proper fusion between the islands, the gap between each island is kept at raster width.

4.3. Specimen Fabrication

The proposed novel infill pattern developed in this study is used as infill pattern for a rectangular block with dimensions of 49mm X 49mm X 15mm. This block has $\frac{H}{L_h}$ layers, where H is the total height of the block and L_h is the layer height and each layer is rotated by 90° to form weave pattern. Table 2 lists the infill parameters for the proposed pattern and the existing Zigzag infill patterns used in this study.
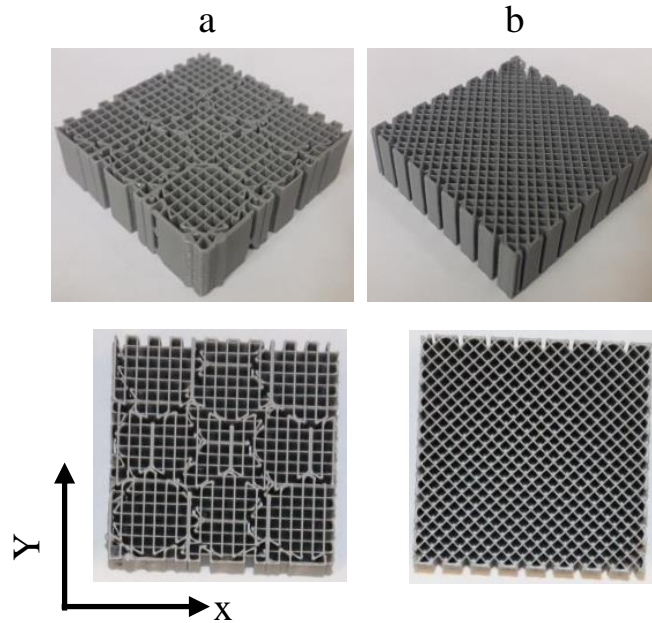
Figure 19: Printed Specimen; a) proposed pattern; b) Zigzag pattern.

To generate the proposed pattern and corresponding G code file, the mathematical model of the proposed infill pattern was implemented in MATLAB R2021a. Besides, the G code for existing zigzag infill pattern was created using the Ultimaker Cura 4.10.0 slicing software. The specimens are printed using a Creality Ender 3 V2 FDM printer with PLA material.

In order to maintain similar weight and raster width the material flow rate of the proposed pattern's raster kept similar to the extrusion rate of the zigzag pattern. All specimens are similar in size, and the printed specimens are excluded of the skin/wall, brim, and any additional support. The temperature of the nozzle and printing bed is maintained at 210°C, and 70°C respectively. All of the specimens are printed with generic PLA having density of 1.24 g/cm^3 as depicted in Figure 19.

Table 2: Process Parameters of the proposed specimens

Hexagonal Zigzag (a)		Zigzag (b)	
Layer height	0.2 mm	Hatch Space	2.1 mm
Specimen Size	49 mm x 49 mm x 15 mm	Specimen Size	49 mm x 49 mm x 15 mm
Zigzag raster quantity in a unit cell, n_r	8	Flow rate	150 %
Hatch Space, h_s	2 mm	Layer height	0.2 mm
1st layer extrusion factor	0.05613	Nozzle diameter	0.4 mm
All other layer's extrusion factor	0.03855		
1st layer speed	1200 mm/min		
All other layer's speed	3000 mm/min		

4.4 Mechanical Testing

Compression tests are performed on an Instron 5967R7526 universal testing machine equipped with a 30 kN load cell to investigate the mechanical behavior of the proposed pattern. The compression tests are carried out at a crosshead speed of 4 mm/min and are terminated at 80% input compressive strain. Instron's BLUEHILL software is used to record the test data. In order to analyze the failure behavior, HD video of each test is recorded through a high-speed camera and photos are taken from the video frames at various compressive strains. The specimens' printing plane is the XY plane, and the build direction is the Z axis.

Due to the crushing load the compressive stress is developed inside the test specimens and is defined by the ratio of the applied load to the perpendicular cross-section area of the specimens. The input compressive strain is calculated through dividing the input deformation by the gauge length along the compression loading direction. For each infill pattern, three specimens are printed and tested. For further analysis such as plotting the stress-strain curve and calculating the elastic moduli, the average test data of the three samples is used.

4.5 Result and Discussion

Figure 20 represents the failure processes of specimens with different infill structures subjected to compression loading. The stress-strain curves for the tests are shown in Figure 21.

Failure occurs when the applied load exceeds the elastic limit of the test specimen, and the nature of the failure varies depending on the type of infill pattern used. Figure 20 depicts the failure mechanisms of the zigzag pattern. It is observed that, at 20% input compressive strain, the collapse begins along the diagonal of the samples depicting the English alphabet "X" as the rasters are oriented parallel to the diagonal that bears the crushing load and the longest rasters at diagonal are prone to buckle. Furthermore, the Movable Cross Head of the UTM machine provides the translation motion for the compression test while the Table is stationary. Once the deformation creates a shear band along the diagonal, the application of the crushing load from the Moveable Cross Head causes the localization of compressive stress at the upper portion of the test specimen. Thus, at 40% input compressive strain, the deformation is localized at the top of the specimen. With the destruction of the upper region, the incremental stress resulting from the crushing load spreads towards the bottom region as depicted at 60% input compressive strain. Once all portions of the test specimen collapse, application of the continuous crushing load causes densification of the sample.

On the other hand, the proposed hexagonal zigzag pattern fails through islands due to the load distribution along island intersections at the boundary. Buckling of raster takes place along individual islands instead of the diagonal failure of the existing zigzag pattern as depicted at 20% input compressive strain in Figure 20. With the increasing crushing load, the deformation spreads toward the neighboring islands. At 40% input compressive strain, the zigzag raster along all islands continues to buckle, and the application of additional crushing load causes uniform deformation

46

throughout the structure. It is observed that the densification of the specimen starts at 60% input compressive strain. The proposed pattern's island failure behavior indicates that the number of islands may influence build part strength, which can be a topic for future research.
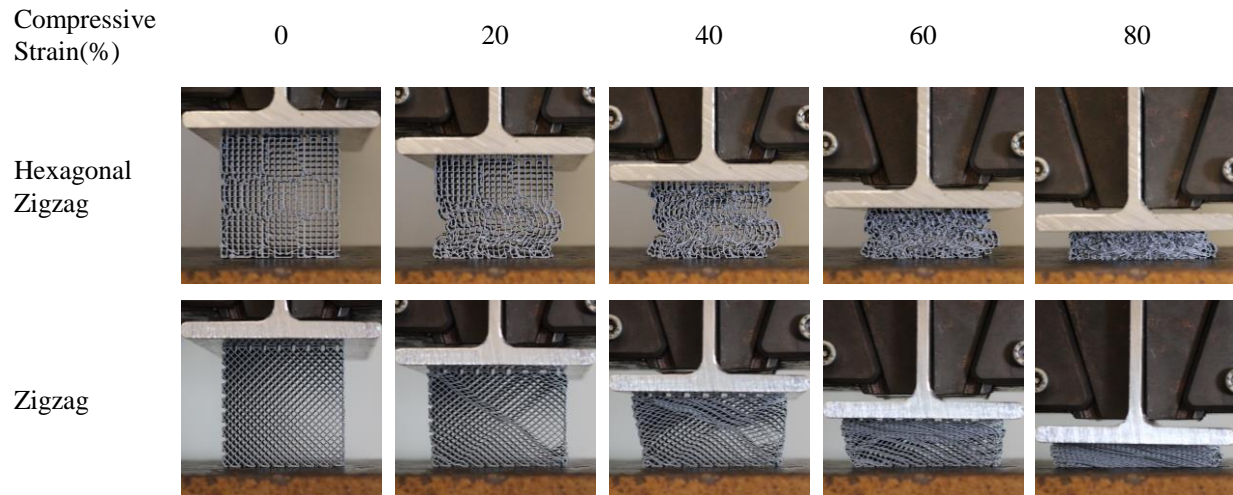
Figure 20: Failure process of the specimen during compression test.

The significant difference between the nature of the zigzag pattern and the proposed pattern is the length of parallel raster. The island's nature reduces the length of the unidirectional raster. The applied compression load acts on the islands and causes the smaller raster to buckle which causes deformation along islands. On the other hand, the long raster covers the unidirectional length for the case of zigzag pattern arranged diagonally which is responsible for diagonal failure.
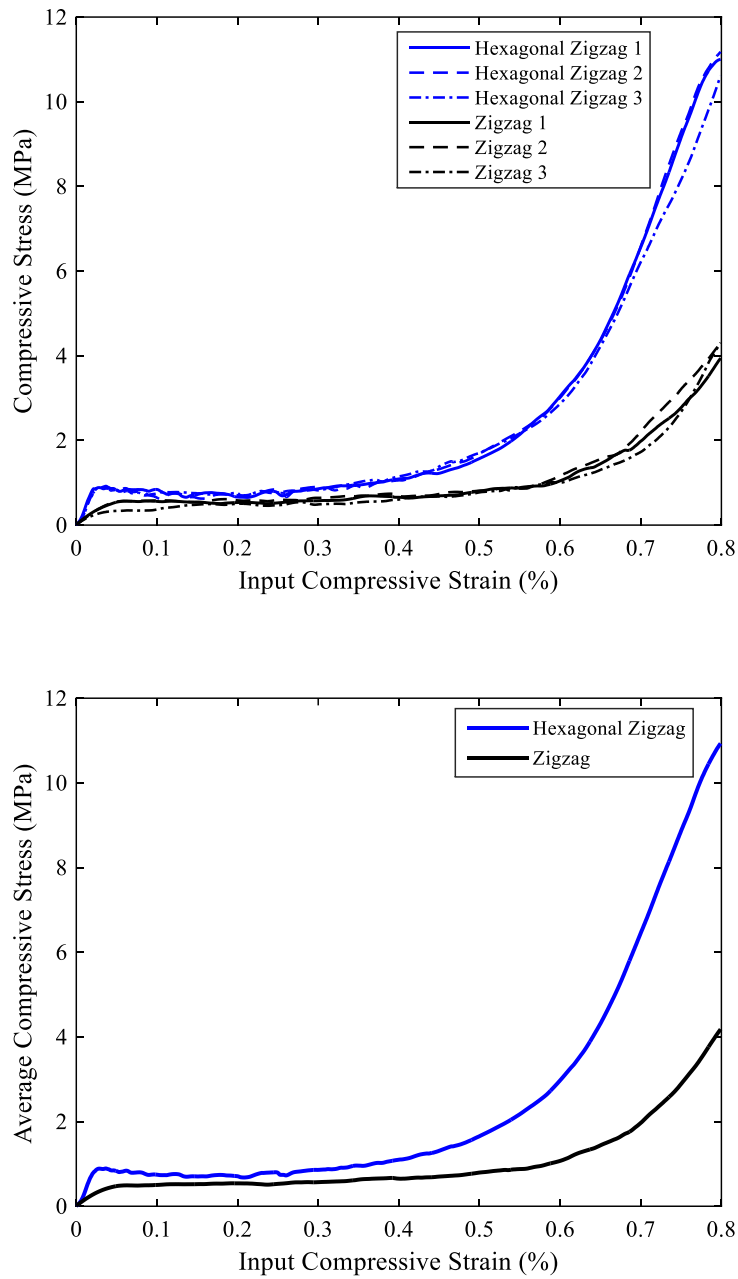
Figure 21: Stress-Strain curve from the compression test of the specimen.

Aside from the failure behavior, the stress-strain curves exhibit the patterns' strength and energy absorption capability. The test specimens' stress-strain curves are divided into three zones: linear elasticity, plateau stress, and densification along input compressive strain. The linear elasticity zone represents the elastic behavior of the specimen that follows the Hook's Law. The

proportional limit describes the maximum compressive stress within the linear elasticity zone. Beyond the proportional limit yielding of the specimen starts which is denoted as compressive yield point [ASTM D695-15]. The plateau stress zone extends from the compressive yield point to the densification start point. The densification start point in this experiment is determined as the initial point of the sharp rise in compressive stress as the rasters are in close contact completely losing the structure strength. Figure 21 depicts the stress-strain curves of the infill patterns that are obtained from the compression tests for each individual test (top) and the average of the three test (bottom).

The maximum strength of the lattices within the elastic limit is described as the compressive strength of the lattice [44]. The proposed infill pattern has a maximum compressive strength of 0.88 MPa compared to the zigzag infill pattern (0.49 MPa) within the elastic limit, as shown in Table 3. In addition, shorter input compressive strain at proportional limit is observed for the proposed hexagonal zigzag patterns, resulting in higher elastic modulus. The elastic modulus in this experiment is calculated from the slope of stress-strain curve within the linear elastic limit as per the ISO13314 Standard. The average stress in the plateau zone, also known as plateau stress [45]. The higher plateau stress of the proposed pattern compared to the zigzag pattern, indicates its resistance to deformation and higher energy absorption capability.

Table 3: Stress-Strain Curve analysis data for the compression test.

Infill Pattern		Hexagonal Zigzag	Zigzag
Linear Elasticity	Max. Compressive Strength (MPa)	0.885	0.492
	Input Compressive Strain (%) at proportional limit	2.7	5.9
	Elastic Modulus (MPa)	32.6	8.1
Plateau	Plateau stress (MPa)	1.16	0.7
Densification	Input Compressive Strain (%)	60	65

Figures 21 and 22 and Table 3 exhibits that the densification begins at 60% and 65% input compressive strain for the proposed and zigzag infill patterns. Furthermore, Figure 21 represents that the proposed infill pattern exhibits greater compressive stress at the densification start point than the zigzag infill pattern. Afterall, the proposed hexagonal zigzag infill pattern has higher compressive strength and plateau stress (in comprehension) compared to the regular zigzag infill pattern and is mechanically promising for 3D printed parts and lightweight structures. It is noted that Figure 22 and Table 3 are prepared on the basis of the average test data of three test sample size and the standard error are calculated using the individual data.
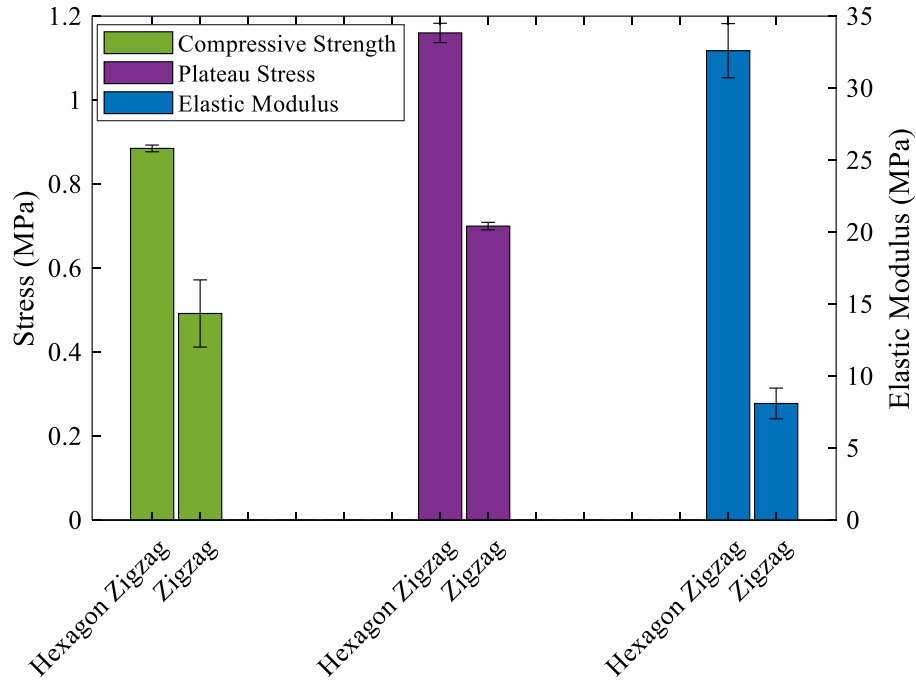
Figure 22: Graphical comparison of the Plateau stress and Elastic Moduli of the infill pattern

4.5.1 Effect of Infill Relative Density on Mechanical Properties

Infill relative density is dictated by the lattice strength and it can be predicted by using Gibson-Ashby model, where the author had established the relationship of the relative elastic modulus, the relative lattice collapse strength (plateau stress) and the densification strain with the relative lattice density as described in Equation 20-22 [46] [47]. The equations predicts the important properties of three zones of the stress strain curve i.e linear elasticity, plateau and densification as described in section 4.5.

$$\frac{E_{lattice}}{E_{solid}} = C_1 \left(\frac{\rho_{lattice}}{\rho_{solid}}\right)^n \tag{20}$$

$$\frac{\sigma_{p.lattice}}{\sigma_{yl.solid}} = C_5 \left(\frac{\rho_{lattice}}{\rho_{solid}}\right)^m \tag{21}$$

$$\varepsilon_D = 1 - \alpha \left(\frac{\rho_{lattice}}{\rho_{solid}} \right) \tag{22}$$

Here, $\frac{E_{lattice}}{E_{solid}}$ is the relative elastic modulus calculated from ratio of the elastic modulus of the lattice, $E_{lattice}$ to the elastic modulus of the solid body, E_{solid}; $\frac{\sigma_{p.lattice}}{\sigma_{yl.solid}}$ is the relative lattice collapse strength calculated from the plateau stress of the lattice, $\sigma_{p.lattice}$ to the yield strength of the solid body, $\sigma_{yl.solid}$; and $\frac{\rho_{lattice}}{\rho_{solid}}$ is the relative lattice density. To present the relationships, the model introduces some prefactors term such as C_1, C_5, and α and exponents term like n and m that depends on the lattice structure type and the material in use. According to Gibson-Ashby the value for C_1, C_5 and α ranges within 0.1~4.0, 0.25~0.35 and 1.4~2.0, respectively while the exponents values for n and m are ~2 and ~3/2 respectively.

In this section, the Gibson-Ashby model is used to figure out the values of the prefactors (C_1, C_5 and α) for the proposed pattern and also compare with the zigzag infill pattern. The established model can be used to predict the plateau stress, $\sigma_{p.lattice}$; elastic modulus, $E_{lattice}$; and densification strain, ε_D for different relative infill density of the proposed infill pattern. The exponent values of n and m are considered 2 and 3/2 respectively. Using information from Table 2 and Equations 15-18 the infill relative density for the proposed infill pattern is calculated as 0.156 (15.6%) and for the similar weight, and similar geometrical dimensions the infill relative density for the zigzag infill pattern is also the same. The relative elastic modulus and relative plateau stress is calculated by using the corresponding information from the conducted experimental data and the standard mechanical properties of the commercial PLA. According to Farah et al. (2016) the elastic modulus and the yield strength of the commercial PLA is 3500 MPa and 70 Mpa respectively [48]. Tables 4 and 5 presents the list of input parameters values and the corresponding calculated values of the prefactors for the proposed infill pattern and zigzag pattern.

It is observed from Table 4 and 5 that the prefactors values for the proposed pattern is higher due to the achievement of better mechanical properties from the experiments. Moreover, the value of C_5 for the proposed pattern is higher than the Zigzag pattern and falls in the small prescribed range that demonstrates the performance of the pattern in terms of the lattice strength and indicates the nature of its higher energy absorption capability. The out-of-range values of α for both infill patterns can be attributed to the material properties.

Table 4: Gibson-Ashby Model analysis for the proposed Hexagonal Zigzag Infill pattern

Hexagonal Zigzag Infill Pattern							
$E_{lattice}$	32.6 MPa	$\sigma_{yl.solid}$	70 MPa	n	2	C_1	0.38
E_{solid}	3500 MPa	ε_D	60 %	m	3/2	C_5	0.27
$\sigma_{p.lattice}$	1.16 MPa	$\frac{\rho_{lattice}}{\rho_{solid}}$	15.6 %			α	2.56

Table 5: Gibson-Ashby Model analysis for the Zigzag Infill pattern

Hexagonal Zigzag Infill Pattern							
$E_{lattice}$	8.1 MPa	$\sigma_{yl.solid}$	70 MPa	n	2	C_1	0.1
E_{solid}	3500 MPa	ε_D	65 %	m	3/2	C_5	0.16
$\sigma_{p.lattice}$	0.7 MPa	$\frac{\rho_{lattice}}{\rho_{solid}}$	15.6 %			α	2.24

Afterall, the values presented in the Tables 4 and 5 can change based on the approximation values of n and m. In order to get the accurate values of the exponent terms, more experiments with different relative infill density need to be conducted and evaluated with data. Despite these limitations the calculated data can be used for rough approximation of the mechanical properties of the proposed infill pattern for different relative infill density.

4.5.2 Mass Distribution

As infill patterns replace the bulk material of the solid body, the mass distribution dictated by the lattice structure influences the position of center of mass of the object. The center of mass affects the weight balance of the printed parts. In this study the center of mass for the proposed infill pattern is calculated by using 3D CAD model and compared with the regular Zigzag infill pattern.

Table 6 represents the location of the center of mass for the proposed infill pattern and the regular Zigzag pattern. Due to the doubling effect of zigzag raster along island intersections, and among the adjacent hexagon unit cells along each island, the mass distribution is not uniform. Furthermore, the size and shape of 'Island 0' and the '$(\lfloor m \rfloor + 1)^{th}$ Island' presented in Figure 18 depends on the size of the hexagon, also influences the location of the center of mass. In Table 6 the centroid and the center of mass are calculated for 49mm X 49mm X 15mm cuboid and their locations are presented based on the co-ordinate system of the CAD program, where Z axis is considered as build direction.

Table 6: Comparison of center of mass location.

Infill Pattern	Hexagonal Zigzag			Zigzag		
Co-ordinate Axes	X	Y	Z	X	Y	Z
Centroid	0.4	0.4	7.6	117.5	117.5	7.6
Center of mass	0.14	0.16	7.6	117.5	117.5	7.6

It is observed that the proposed pattern has shifted the center of mass along 0.35 mm by 222.7° with respect to the centroid point in the XY plane. Moreover, the center of mass locations for odd and even layers presented in Table 7 describes that the center of mass has shifted by 0.92 mm at

an angle of 157.6º and 292.4º respectively from the centroid point. The reduction in distance between the overall center of mass and centroid point demonstrates the mitigating effect of 90º layer rotation strategy on mass distribution. On the other hand, the Zigzag infill pattern does not shift the center of mass from centroid position indicating its uniform mass distribution nature.

Table 7: Center of mass information for different layers.

Infill Pattern	Odd Layer		Even Layer	
Co-ordinates	X	Y	X	Y
Controid	0.4	0.4	0.4	0.4
Center of mass	-0.45	0.75	0.75	-0.45

4.6 Chapter Conclusion

The study introduces a novel hybrid infill pattern that combines the features of traditional zigzag and honeycomb patterns to achieve better manufacturability and improved mechanical performance. The mechanical test results exhibit that the proposed infill pattern gets deformed through individual islands. In comparison to the regular zigzag infill pattern, the proposed infill pattern exhibits higher compressive strength, plateau stress and elastic modulus. Furthermore, by adjusting the infill structure parameters, the relative infill density and the hexagon cell size of the proposed infill pattern can be controlled. Future studies can be conducted to investigate the effect of hexagon cell size on the compressive strength and failure behavior of the proposed infill pattern for the same relative infill density.

CHAPTER FIVE: CONCLUSION

In this thesis two separate studies are conducted for two different AM technologies. The effects of material deposition strategies have been investigated. The first study of this thesis focuses on LPBF technology where a novel scan pattern is modeled, and the corresponding residual stress is compared with the existing scan patterns. The second study of this thesis concentrates on FDM technology where a novel infill pattern is developed, and its mechanical behaviors are explored and compared with existing infill patterns.

The first study concludes that the residual stress developed in a build part generated from the thermal gradient and rapid solidification is greatly influenced by the scan patterns. As the tiny moving heat source is responsible for uneven heating of the build part, optimizing the travel route can play a vital role in reducing thermal gradient, rapid solidification and thus the residual stress. In this study the proposed scan pattern exhibits relatively lower residual stresses due to its uniform thermal distribution and re-heating strategy as compared to the other existing scan patterns. As the simulation result exhibits the higher tensile residual stress components due to ignoring the plastic strain, incorporating the inherent strain model will increase the accuracy of the result.

On the other hand, the second study concludes that the infill pattern widens the scope of producing lightweight porous object with desired mechanical integrity. In this study a novel infill pattern is developed, and its mechanical characteristics are explored and compared with other existing infill patterns. The proposed novel infill pattern demonstrates higher compressive strength, plateau stress, and elastic modulus as compared to the existing Zigzag infill pattern. The different mechanical characteristics of this novel infill pattern broaden the scope of a designer's choice. Afterall, different patterns demonstrate their performance in corresponding applications.

56

REFERENCES

1. Aldo, H., *A Review of AdditiveManufacturing.* 2012.

2. Cooke, S., et al., *Metal additive manufacturing: Technology, metallurgy and modelling.* Journal of Manufacturing Processes, 2020. **57**: p. 978-1003.

3. Song, J., et al., *Role of scanning strategy on residual stress distribution in Ti-6Al-4V alloy prepared by selective laser melting.* Optik, 2018. **170**: p. 342-352.

4. Chen, Q., et al., *A level-set based continuous scanning path optimization method for reducing residual stress and deformation in metal additive manufacturing.* Computer Methods in Applied Mechanics and Engineering, 2020. **360**: p. 112719.

5. Promoppatum, P. and S.-C. Yao, *Influence of scanning length and energy input on residual stress reduction in metal additive manufacturing: Numerical and experimental studies.* Journal of Manufacturing Processes, 2020. **49**: p. 247-259.

6. Chen, C., et al., *Effect of overlap rate and pattern on residual stress in selective laser melting.* International Journal of Machine Tools and Manufacture, 2019. **145**: p. 103433.

7. Kemerling, B., et al., *Residual stress evaluation of components produced via direct metal laser sintering.* Welding in the World, 2018. **62**(3): p. 663-674.

8. Sezer, H., et al. *Mathematical Modeling of Thermal Behavior in Layer-by-Layer Part Fabrication by Direct Metal Laser Sintering Process for Different Scanning Patterns*. in *International Manufacturing Science and Engineering Conference*. 2020. American Society of Mechanical Engineers.

9. Kudzal, A., et al., *Effect of scan pattern on the microstructure and mechanical properties of Powder Bed Fusion additive manufactured 17-4 stainless steel.* Materials & Design, 2017. **133**: p. 205-215.

10.	Qiu, C., et al., *On the role of melt flow into the surface structure and porosity development during selective laser melting.* Acta Materialia, 2015. **96**: p. 72-79.

11.	Kou, S., *Welding metallurgy.* New Jersey, USA, 2003. **431**(446): p. 223-225.

12.	Murr, L.E., et al., *Metal fabrication by additive manufacturing using laser and electron beam melting technologies.* Journal of Materials Science & Technology, 2012. **28**(1): p. 1-14.

13.	Zhang, B., Y. Li, and Q. Bai, *Defect formation mechanisms in selective laser melting: a review.* Chinese Journal of Mechanical Engineering, 2017. **30**(3): p. 515-527.

14.	Singh, S., S. Ramakrishna, and R. Singh, *Material issues in additive manufacturing: A review.* Journal of Manufacturing Processes, 2017. **25**: p. 185-200.

15.	Kings, T.H.E., *"Advanced mechanics of materials" 5th edition, A.P. Boresi, R.J. Schmidt and O.M. Sidebottom.* Strain, 1993. **29**(4): p. 141-142.

16.	Sames, W.J., et al., *The metallurgy and processing science of metal additive manufacturing.* International materials reviews, 2016. **61**(5): p. 315-360.

17.	Koepf, J.A., et al., *3D multi-layer grain structure simulation of powder bed fusion additive manufacturing.* Acta Materialia, 2018. **152**: p. 119-126.

18.	Akram, J., et al., *Understanding grain evolution in additive manufacturing through modeling.* Additive Manufacturing, 2018. **21**: p. 255-268.

19.	Mercelis, P. and J.P. Kruth, *Residual stresses in selective laser sintering and selective laser melting.* Rapid Prototyping Journal, 2006. **12**(5): p. 254-265.

20.	Shiomi, M., et al., *Residual stress within metallic model made by selective laser melting process.* CIRP Annals, 2004. **53**(1): p. 195-198.

21. Liu, Z., et al., *A critical review of fused deposition modeling 3D printing technology in manufacturing polylactic acid parts.* The International Journal of Advanced Manufacturing Technology, 2019. **102**(9): p. 2877-2889.

22. Soltani, A., et al., *3D printing on-water sports boards with bio-inspired core designs.* Polymers, 2020. **12**(1): p. 250.

23. Nazmul Ahsan, A. and B. Khoda, *Characterizing novel honeycomb infill pattern for additive manufacturing.* Journal of Manufacturing Science and Engineering, 2021. **143**(2).

24. Chacón, J., et al., *Additive manufacturing of PLA structures using fused deposition modelling: Effect of process parameters on mechanical properties and their optimal selection.* Materials & Design, 2017. **124**: p. 143-157.

25. Wang, K., et al., *Effects of infill characteristics and strain rate on the deformation and failure properties of additively manufactured polyamide-based composite structures.* Results in Physics, 2020. **18**: p. 103346.

26. Ahsan, A.M.M.N., M.A. Habib, and B. Khoda, *Resource based process planning for additive manufacturing.* Computer-Aided Design, 2015. **69**: p. 112-125.

27. Ahsan, N. and B. Khoda, *AM optimization framework for part and process attributes through geometric analysis.* Additive Manufacturing, 2016. **11**: p. 85-96.

28. Hussin, M.S., et al. *Experimental and finite element modeling of partial infill patterns for thermoplastic polymer extrusion 3D printed material using elasto-plastic method.* in *AIP Conference Proceedings*. 2020. AIP Publishing LLC.

29. Abbas, T., F.M. Othman, and H.B. Ali, *Effect of infill Parameter on compression property in FDM Process.* dimensions, 2017. **12**(12.7): p. 25.4.

30. Subeshan, B., et al. *Investigating compression strengths of 3D printed polymeric infill specimens of various geometries*. in *Nano-, Bio-, Info-Tech Sensors, and 3D Systems II*. 2018. SPIE.

31. Deb, J., N. Ahsan, and S. Majumder. *Modeling the interplay between process parameters and part attributes in additive manufacturing process with artificial neural network*. in *ASME 2022 International Mechanical Engineering Congress and Exposition (IMECE2022)*. 2022. Columbus, Ohio: ASME.

32. Fernandez-Vicente, M., et al., *Effect of infill parameters on tensile mechanical behavior in desktop 3D printing.* 3D printing and additive manufacturing, 2016. **3**(3): p. 183-192.

33. Aloyaydi, B., S. Sivasankaran, and A. Mustafa, *Investigation of infill-patterns on mechanical response of 3D printed poly-lactic-acid.* Polymer Testing, 2020. **87**: p. 106557.

34. Yao, T., et al., *A method to predict the ultimate tensile strength of 3D printing polylactic acid (PLA) materials with different printing orientations.* Composites Part B: Engineering, 2019. **163**: p. 393-402.

35. Ding, D., et al., *A tool-path generation strategy for wire and arc additive manufacturing.* The International Journal of Advanced Manufacturing Technology, 2014. **73**(1): p. 173-183.

36. Yan, W., Z. Yue, and J. Feng, *Study on the role of deposition path in electron beam freeform fabrication process.* Rapid Prototyping Journal, 2017.

37. Eftekhari, A., et al., *FVTool: a finite volume toolbox for Matlab*. 2015.

38. Sezer, H., et al., *Modeling Residual Thermal Stresses in Layer by Layer Formation of Direct Metal Laser Sintering Process for Different Scanning Patterns.* Rapid Prototyping Journal, 2022. **In Press**.

39. Tang, J., et al., *Modeling Maximum Stresses in Each Layer for Layer-by-layer Deposition of the Direct Metal Laser Sintering Processes for Different Scanning Patterns.*, in *ASME Manufacturing Science and Engineering Conference*. 2022: West Lafayette, Indiana.

40. Yan, F.K., et al., *Strength and ductility of 316L austenitic stainless steel strengthened by nano-scale twin bundles.* Acta Materialia, 2012. **60**(3): p. 1059-1071.

41. Wang, Y.M., et al., *Additively manufactured hierarchical stainless steels with high strength and ductility.* Nature materials, 2018. **17**(1): p. 63-71.

42. Smith, W.L., et al., *Residual stress analysis of in situ surface layer heating effects on laser powder bed fusion of 316L stainless steel.* Additive Manufacturing, 2021. **47**: p. 102252.

43. Williams, R.J., et al., *Effects of heat treatment on residual stresses in the laser powder bed fusion of 316L stainless steel: Finite element predictions and neutron diffraction measurements.* Journal of Manufacturing Processes, 2020. **57**: p. 641-653.

44. Saleh, M., et al., *Compression Performance and Failure Analysis of 3D-Printed Carbon Fiber/PLA Composite TPMS Lattice Structures.* Polymers, 2022. **14**: p. 4595.

45. Maskery, I., et al., *An investigation into reinforced and functionally graded lattice structures.* Journal of Cellular Plastics, 2016. **53**(2): p. 151-165.

46. Gibson, L.J. and M.F. Ashby, *Cellular Solids: Structure and Properties*. 2 ed. Cambridge Solid State Science Series. 1997, Cambridge: Cambridge University Press.

47. Ashby, M., et al., *Metal Foams: a Design Guide.* Materials & Design, 2002. **23**: p. 119.

48. Farah, S., D.G. Anderson, and R. Langer, *Physical and mechanical properties of PLA, and their functions in widespread applications—A comprehensive review.* Advanced drug delivery reviews, 2016. **107**: p. 367-392.